Chapter 6
Nanophotonics

Abstract Single crystalline semiconductor NWs have been extensively investigated as building blocks for ultra-small and entirely new electronic and photonic devices, due to their unique electronic and optical properties. The sub-wavelength diameters of NW structures and tunable energy band gaps provide a host of advantages for investigating generation, detection, amplification and modulation of light. Photonic platforms using NW building blocks also offers the promise of integrated functionalities at dimensions compatible with top-down fabricated electronics. With rational design and synthesis of the NW structures, the capability of controlling and manipulating these structures on surface to form single devices and networks is a crucial step for realizing these chemically synthesized NWs into photonic circuitry. In this chapter we will review progress made in the area of NW photonic devices, including waveguides, light-emitting diodes, lasers, and photodetectors.

6.1 Introduction

The field of photonics in essence focuses on the control of photons in free space or in matter [1]. Manipulation of photons in semiconductor bulk crystals and thin films has culminated in breakthroughs such as light-emitting diodes (LEDs) and lasers [2]. With the shrinking of devices to smaller length scales in the microelectronics industry, the continuing success of photonic technologies also relies on the discovery of new optical materials, integration strategies and the miniaturization of optoelectronic devices for better performance, lower cost and lower power consumption. Although state-of-the-art lithography technologies are capable of fabricating nanostructured features and functionalities [3], chemically grown NWs still posses unique advantages, including single-crystalline, diameter and morphology controlled structures with near atomically smooth surfaces, as well as the potential for hetero-integration with electronics and other materials via bottom-up assembly [4–7]. NW photonics is a particularly exciting frontier due to the ability to precisely control NW composition and hence the resulting bandgap, which cannot be

A. Zhang et al., *Nanowires*, NanoScience and Technology,
DOI 10.1007/978-3-319-41981-7_6

accomplished with CNTs, and using a combination of nanolithography tools, it is possible to assemble photonic circuits with designed functions [8–13]. NWs synthesized from direct bandgap semiconductors have shown tremendous promise for assembling subwavelength nanophotonic devices for the generation, waveguiding, and detection of light at the nanoscale [10]. Nanophotonic devices such as optically-pumped and electrically-driven NW lasers, waveguides, light emitting diodes (LEDs), photodetectors, have been successfully demonstrated [8, 9, 11–13]. In addition to miniaturization of devices, NW-based photonic systems can provide many interesting and novel device concepts in comparison to planar technology. The potential for co-assembling nanoscale light sources and detectors, fabricated from a variety of different materials, opens up unique opportunities for integrated photonic systems as well as the integration of nanophotonic systems with silicon micro- and nano-electronics [14]. In this chapter, we will discuss the optical properties, including photoluminescence and nonlinear responses, of semiconductor NWs, and review the significant progress made in the field of semiconductor NW photonic devices. Other comprehensive reviews of NW photonics can be found in [8, 12, 13].

6.2 Optical Phenomena

6.2.1 Photoluminescence from Nanowire Structures

Photoluminescence (PL) is a light emission process in which a substance absorbs and then re-radiates photons. PL data collected from individual direct-bandgap NWs can reveal a wealth of information, both in terms of characterization of the materials and optical properties, such as band-edge emission, trap states, radiative efficiency, carrier and photon confinement [8, 10]. In this section, we briefly introduce PL from homogeneous NWs and NW heterostructures.

6.2.1.1 Homogeneous Nanowires

The optical properties of homogeneous NWs, including GaAs [15–17], InP [18, 19], GaN [20], ZnO [21], ZnS [22], ZnSe [23], CdS [24], CdSe [25], Si [26], have been extensively studied by steady state and transient PL spectroscopy. The results from these studies show that individual growth methods and conditions can strongly affect NW optical properties in terms of emission intensity, spectral width and peak position, and the presence of long wavelength components from impurity states that emit radiatively. High quality NWs synthesized under controlled conditions at high temperatures typically emit brightly with a spectral peak near the band edge. The width of the PL spectra at room temperature reveal critical information about the quality of the NWs with narrower widths (~20–30 nm)

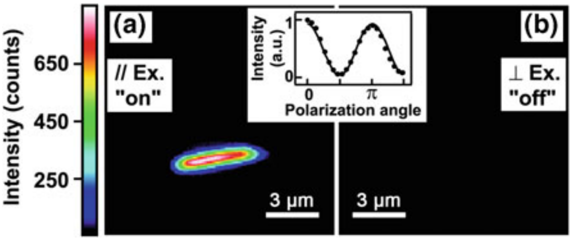

Fig. 6.1 **a** PL image of a single 20-nm InP NW with the exciting laser polarized along the wire axis. **b** PL image of the same NW as in (**a**) under perpendicular excitation. *Inset*, variation of overall PL intensity as a function of excitation polarization angle with respect to the NW axis. Reproduced from [18]. Copyright 2001 the American Association for the Advancement of Science

corresponding to high optical quality of NWs. The narrower widths can be attributed to lower defect density within and at the passivated surfaces of the NWs [8].

Optical absorption and emission from NWs have been found to be predominantly polarized along the long axis of the wires [18, 27]. The observed polarization anisotropy can be explained from a purely classical perspective as arising from the anisotropic geometry of the NWs—where the NW diameter is much smaller than the wavelength of light but the length is much larger—and also due to the large dielectric mismatch between a free standing NW and its surrounding environment [18]. PL images of single InP NWs recorded at room temperature with the polarization of the exciting laser both parallel (Fig. 6.1a) and perpendicular (Fig. 6.1b) to the NW showed a large polarization anisotropy with the observed PL turning from "on" to "off" as the excitation polarization was rotated from parallel to perpendicular. Integration of the emission as a function of excitation angle showed that the intensity exhibited the expected periodic dependence on angle (Fig. 6.1, inset).

6.2.1.2 Axial Heterostructures

PL measurements provide a unique means to verify quantum confinement of charge carriers in NW heterostructures. PL studies have been carried out for several II–VI and III–V direct-gap systems, including ZnSe–CdSe [28], ZnO–ZnMgO [29], InAs–GaAs [30], InAs–InP [31] and AlGaN–GaN [32]. Park et al. [29] observed a clear blue-shift in the PL peak energy of ZnO–ZnMgO nanorod heterostructures with decreasing ZnO well width, demonstrating quantum confinement in the axial direction. Panev et al. [30] observed sharp exciton emission from InAs quantum dots inside GaAs NW hosts. The peak energies emitted by the InAs dots were substantially blue shifted from bulk InAs, indicating that substantial alloying with the GaAs NW occurred. Accordingly, the effects of possible confinement potentials on the peak energy could not be determined. Poole et al. [31] synthesized InP–InAs–InP NWs on InP substrates without catalyst. During PL excitation at low power densities, a single well-defined peak is observed at 921 meV. At higher power densities, excited state peaks are observed at energy spacings consistent with the quantum confinement of excitons within the estimated well widths. More recently, Holmes et al. [32] demonstrated triggered single photon emission at room temperature from a site-controlled III–nitride quantum dot embedded in a NW. The photon statistics are found to be insensitive to temperature, in contrast to other QD-based triggered single photon emitters which exhibit a pronounced degradation at elevated temperatures. Arrays of such single photon emitters were proposed for room-temperature quantum information processing applications such as on-chip quantum communication [32].

6.2.1.3 Radial Heterostructures

Confinement and quantum confinement effects in radial NW heterostructures have also been verified by PL spectra [33–35]. In 2004, Qian et al. [33] obtained PL spectra from *n*-GaN/InGaN/*p*-GaN core/shell/shell (CSS) structures, exhibiting a dominant emission peak at 448 nm. This wavelength is consistent with band-edge emission from an InGaN structure of composition $\mathrm{In_{0.18}Ga_{0.82}N}$. The InGaN emission is approximately 20 times stronger than the small GaN band-edge emission peak also present in the PL spectrum, which shows that the much smaller volume InGaN shell in the CSS structures provides an efficient region for radiative recombination. In 2008, the same group [34] reported the growth of highly uniform $(\mathrm{InGaN/GaN})_n$ multi-quantum-well (MQW) core/shell NW heterostructures, with $n = 3$, 13 and 26 and each InGaN well thicknesses of 1–3 nm (Fig. 6.2a). PL spectra from individual 26-MQW NWs containing different indium compositions are displayed in Fig. 6.2b, c. It can be seen that the InGaN emission peak red-shifts from 382 to 440 and then to 484 nm (Fig. 6.2c) with increasing indium composition. The peak broadening with In% is consistent with InGaN planar structures. Later, the synthesis of AlN/GaN MQW NW structures has also been demonstrated. The observed blue-shifted emission of PL spectra was attributed to the quantum confinement in the GaN layers [35].

6.2.2 *Nonlinear Processes*

In linear optics, the dielectric polarization P depends linearly to the electric field, E, of the light, $P = \varepsilon_0\chi^{(1)}E$, where $\chi^{(1)}$ is the first order susceptibility tensor and ε_0 is the vacuum permittivity. While this consideration is sufficient at low incident field strengths, when the field strength increases it is possible for higher order terms to be important. In general, P can be expressed as a series expansion in powers of E as:

$$P = P^{(1)} + P^{(2)} + P^{(3)} + \cdots = \varepsilon_0\left[\chi^{(1)}E + \chi^{(2)}E^2 + \chi^{(3)}E^3 + \cdots\right]$$

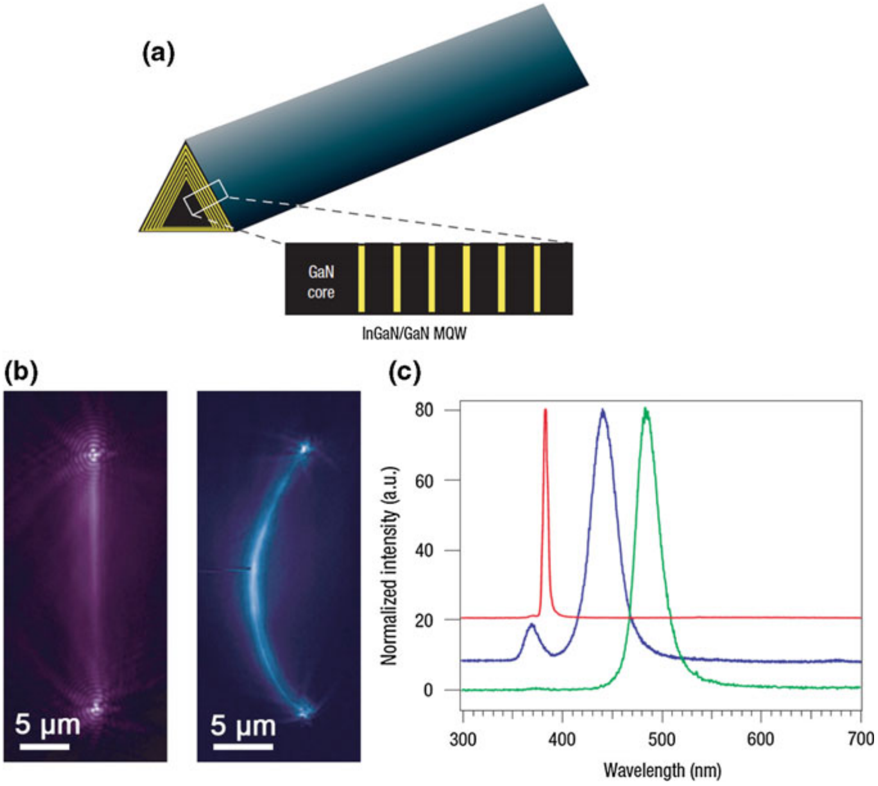

Fig. 6.2 **a** Schematic diagram of an MQW NW. The InGaN layer is indicated in *yellow color*. **b** PL images (*false color*) recorded from GaN/$In_{0.05}Ga_{0.95}N$ (*left*) and GaN/$In_{0.23}Ga_{0.77}N$ (*right*) MQW NW structures. **c** PL spectra collected from three representative 26MQW NW structures with increasing In composition. Reproduced from [34]. Copyright 2008 Nature Publishing Group

where $\chi^{(2)}$ and $\chi^{(3)}$ are the second- and third-order nonlinear optical susceptibilities [36, 37]. Nonlinear optical (NLO) processes are often referred to as "N wave mixing" where N is the number of photons involved (including the emitted one). Many nanostructures exhibit strong intrinsic NLO signals under tight focusing conditions. Combining NLO signals with scanning microscopy has generated an array of label-free imaging modalities for material and biological studies [38, 39]. Unlike linear optical microscopy, NLO microscopy offers inherent 3D spatial resolution, relatively large optical penetration into tissues with near infrared (NIR) excitation, and reduced photo-damage due to reduced optical interaction with endogenous molecules [38, 39]. This section introduces different NLO processes in semiconductor NWs (Fig. 6.3), including second harmonic generation (SHG), third-harmonic generation (THG), four-wave mixing (FWM), and stimulated Raman scattering (SRS), with an emphasis on SHG.

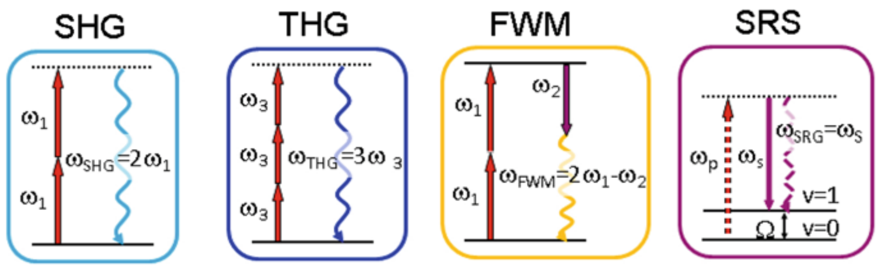

Fig. 6.3 Energy diagrams of NLO modalities. *Solid lines* represent electronic and vibrational states of molecules, *dashed lines* are virtual states. The *straight arrows* are excitation beams, the *wavy arrows* are output signal beams. The *gray arrows* represent relaxation in electronically excited states. ω_1 and ω_2 are excitation beams. Ω is the frequency of vibrational transition between vibrational ground state and vibrationally excited state. Reproduced from [38]. Copyright 2011 John Wiley and Sons

6.2.2.1 Second Harmonic Generation

SHG is a second-order NLO process in which two incident photons (ω_1) are converted to one scattered photon ($2\omega_1$) with energy equal to the sum of the excitation photons. Since all even-order nonlinear susceptibilities $\chi^{(n)}$ vanish in centrosymmetric media, SHG cannot occur in materials with inversion symmetry, such as bulk Si [36, 37]. As the excitation beam and SHG have different wavelength in the same material, if no specific measures are taken, there will be a phase mismatch, where the phase difference $\Delta\varphi$ after propagating a distance z will be $\Delta\varphi = (k_{2\omega} - 2\ k_{\omega})z$, where $k_{2\omega}$ and k_{ω} are wave vectors at frequencies $2\omega_1$ and ω_1. The efficient generation of SHG requires phase matching, $\Delta\varphi = 0$, over the whole length of the material, L, otherwise SHG waves will interfere destructively, resulting in decreased intensity [36, 37]. If $\Delta\varphi$ is very small, SHG waves can add constructively over a coherence length $L_c = \lambda/2(n_{2\omega} - n_{\omega})$, where λ is the excitation wavelength, and $n_{2\omega}$ and n_{ω} are refractive indices corresponding to the excitation and SHG wavelengths. The most commonly used crystals for nonlinear optics are birefringent (e.g. $LiNbO_3$), in which the phase matching condition can be achieved by propagating the beams at different frequencies as ordinary or extraordinary rays [36, 37]. It is important to note that the wave vectors of pump and SHG are always nonparallel, i.e., phase matching is not formally possible in 1D in bulk materials.

Although the generation of SHG requires non-centrosymmetric structures, the broken symmetry at the surface of NWs and the mismatch of dielectric constants at the interface of NWs and the environment can cause SHG even in materials with a high symmetry crystal lattice [40]. In addition, NWs with diameters much smaller than the incident wavelengths can act as subwavelength waveguides that radially confine optical modes, with increased L_c and therefore a longer effective length over which 1D nonlinear process takes place [41]. Furthermore, the intensity of the optical electric field inside illuminated NWs can depend dramatically on the NW orientation relative to the excitation light polarization, with the maximum relative amplitude at the electric-field polarization oriented along the NWs [40].

Many types of NWs have been reported to be able to emit SHG signals [41–48]. As an example, Nakayama et al. [44] reported the development of continuously tunable coherent visible light source from individual $KNbO_3$ NWs, which exhibited efficient SHG and acted as frequency converters, allowing for the local synthesis of a wide range of colors via sum and difference frequency generation. As shown in Fig. 6.4a, single $KNbO_3$ NWs were optically trapped using an infrared optical tweezer with the trap wavelength at 1064 nm. A diffraction-limited spot is observed by an electron-multiplying charge-coupled device (CCD) at the distal end of the wire, revealing optical waveguiding away from the site of photon conversion and

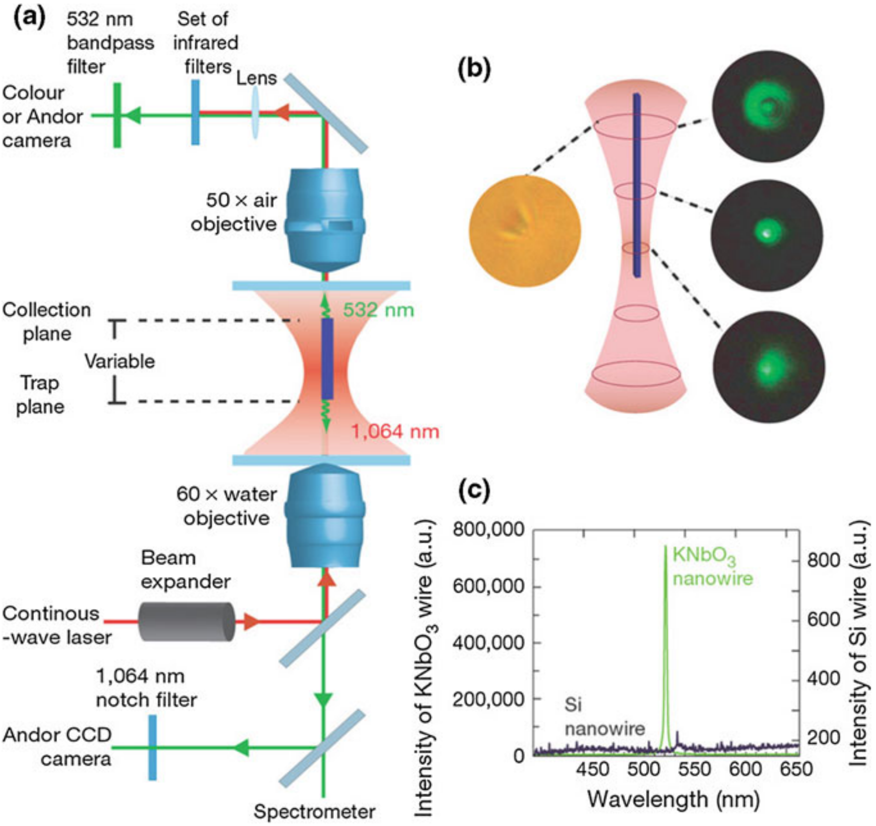

Fig. 6.4 **a** Detailed set-up for the single-beam optical trapping instrument. **b** Bright field (*left*) and SHG (*right*) images of the trapped $KNbO_3$ NW. Waveguiding of the SHG signal (*green*) leads to diffraction rings at the distal (*top*) end of the NW which acts as a subwavelength aperture. **c** Observed spectra for $KNbO_3$ and SiNWs. Strong SHG signal is collected from the trapped $KNbO_3$ NW (*green, left axis*), while no signal was observed from SiNWs (*black, right axis*). Reproduced from [44]. Copyright 2007 Nature Publishing Group

emission from the aperture defined by the NW cross-section (Fig. 6.4b). Spectral analysis reveals that the light is green with a wavelength of 531 ± 1.8 nm (Fig. 6.4c), matching well with the expected SHG signal given a trapping/pump wavelength of 1,064 nm, this SHG might originate from both the bulk and the surface of the NW. In another report [46], SHG was experimentally observed from periodic arrays of vertical GaP nanopillars. Polarization of the measured light was used to distinguish between the bulk and surface SHG signals. For larger diameters (250 nm), it is mainly the bulk nonlinearity which contributes to the SHG, the polarization of SHG is predominantly orthogonal to that of the pump; while for smaller diameters (150 nm), the surface contribution becomes significant, the polarization of the SHG signal is predominantly parallel to the pump.

6.2.2.2 Third-Harmonic Generation and Four-Wave Mixing

THG and FWM are third-order NLO processes and are not limited to non-centrosymmetric structures [36, 37]. THG requires three photons (ω_1) in order to generate one photon at the tripled frequency ($3\omega_1$) [49–51], while for FWM, three incident laser fields with frequencies of ω_1, ω_2, ω_3 interact with the material's $\chi^{(3)}$ to generate a signal field at a frequency of ω_4 [50, 52–54]. Similar to SHG, the generation of THG and FWM also requires phase matching. As an example, Jung et al. [50] observed strong emission of THG signal from SiNWs of 40 nm diameters (Fig. 6.5a). The THG emission spectra recorded from individual NWs in the 400–680 nm region display a peak at 428 nm, in agreement with the emission wavelength of THG, 430 nm, produced by a 1290-nm excitation. The THG intensity exhibits a periodic dependence on the angle θ: the signal intensity arising from the perpendicular polarization is much smaller than that from parallel polarization. In addition, THG intensity of the SiNWs remains consistent over the time (Fig. 6.5b). The authors [50] also observed a very strong FWM response along the long axis of SiNWs (Fig. 6.5c), with the peak positioned at 645 nm, in agreement with the emission wavelengths of FWM generated by collinearly combined pump field (790 nm) and Stokes field (1018 nm). The FWM signal from these nanomaterials is brighter than the nonresonant FWM contribution from the biological material itself, which enables identification of SiNW probes in live cells and tissues. As a proof of concept, the authors monitored blood circulation of PEGylated SiNWs in live animals and mapped the distribution of SiNWs in organs after systemic clearance (Fig. 6.5d, e).

6.2.2.3 Stimulated Raman Scattering

In spontaneous Raman scattering, a pump laser at a frequency ω_p illuminates the sample, and the sample emits photons at the Stokes and anti-Stokes frequencies, ω_s and ω_{as}, due to inelastic scattering. However, if one additional laser with frequency ω_s (Stokes beam) coincide with ω_p on the sample, the Raman signal with ω_s

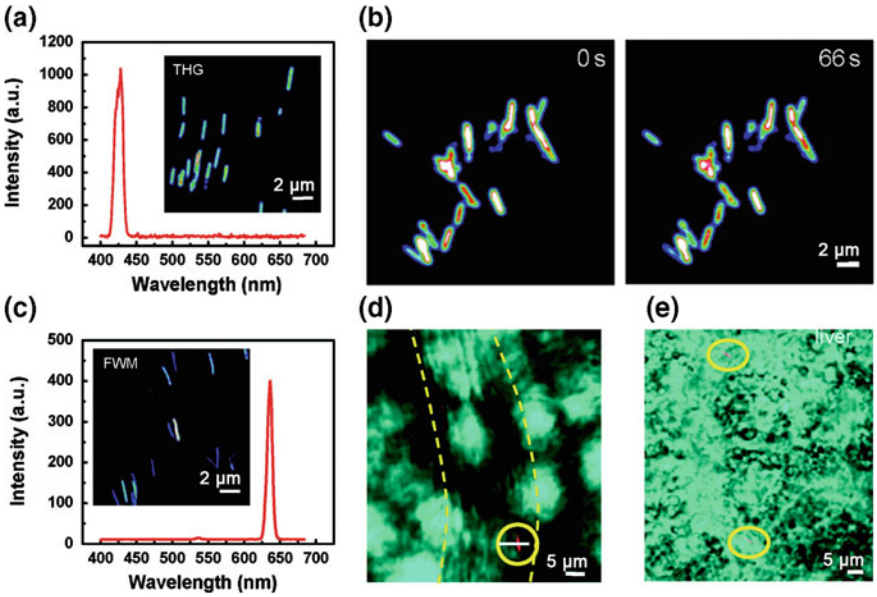

Fig. 6.5 **a** THG image and spectrum from SiNWs, excited by a 1290 nm laser. **b** THG images of SiNWs acquired at different scanning time. **c** FWM image and spectrum from SiNWs. **d** FWM imaging of PEGylated SiNWs (*red*) flowing in a blood vessel (outlined by *dashed yellow line*) in the earlobe of a living mouse. **e** FWM imaging of SiNWs (*red*) in liver after systemic clearance in a mouse. Reproduced from [50]. Copyright 2009 American Chemical Society

frequency is largely amplified, therefore this process is called SRS. The intensity of spontaneous Raman is proportional to pump power, but smaller by many orders of magnitude, while the intensity of SRS depends nonlinearly on incident intensity, and can be comparable to the pump intensity [55, 56]. When the length of the NW becomes comparable to wavelength of light, the NW behaves similar to a cavity, so that inelastic photons may form standing waves confined by the NW cavity. As a result, SRS becomes possible. For example, Wu et al. [57] measured the integrated Raman–Stokes intensity of transverse optical (TO) phonon band versus laser power for a series of GaP NWs with length between 200 nm and 3.3 µm. It was found that as the NW length decreases, the nonlinear effect becomes dominant. For NWs longer than ~2 µm, the Raman intensity is approximately a linear function of laser power up to 1 mW, a characteristic of spontaneous (linear) Raman scattering. For powers over 1 mW, laser-induced heating is shown. For NWs shorter than 1.1 µm, Raman scattering exhibits spontaneous characteristics ($I_{\mathrm{TO}} \propto P$) at lower laser power; however, above a threshold power (P_{T}), a strong nonlinear behavior $I_{\mathrm{TO}} \propto P^n$ is observed, where the exponent n grows rapidly as the length decreases to a value ~ 4.3 for the shortest segment of 270 nm. Another interesting observation is that P_{T} decreases as the length decreases. Further studies of these interesting results are certainly warranted and could open unique research and application opportunities.

6.3 Photonic Devices

6.3.1 Nanowire Waveguides

In order to assemble light-based devices into highly-integrated photonic circuits, an important step is to develop NW waveguides that can transport light over relatively large distances from one part of a chip to another, and provide flexible interconnection patterns needed to carry out complex tasks. In this section, we describe NW waveguides with bends/twists. In 2003, Tong et al. [58] used a flame-heated fiber drawing method to fabricate long free-standing silica NWs with diameters down to 50 nm and lengths up to tens of millimeters. The NWs did not break when being bent/twisted, indicating their excellent flexibility and mechanical properties. Light was launched into these NWs by optical evanescent coupling. The NWs allowed single-mode operation, and had an optical loss of less than 0.1 dB mm^{-1}. Barrelet et al. [59] carried out quantitative studies of CdS NW structures showing that light propagation takes place with only ca. 1 dB loss or less per abrupt bend, after accounting for loss in the straight portion of the NW. In addition, light can be guided and coupled efficiently through the sharp bends or turns, defined by crossed NWs and end-to-end assembled NWs. In 2004, Yang and coworkers [60] used SnO_2 nanoribbons as subwavelength waveguides for light with energies less than SnO_2 bandgap. Freestanding nanoribbons were repeatedly and elastically curved into loops with radii as small as 5 μm. On appropriately chosen surfaces, single nanoribbons were easily fashioned into a variety of shapes with the help of NW–substrate forces to prevent elastic recoil. Depending on ribbon cross-sectional area and the density of scattering centers, these nanoribbons demonstrated efficient waveguiding with losses from 1–8 dB/mm at a wavelength of 450–550 nm. Furthermore, because of their remarkable mechanical flexibility, the SnO_2 nanoribbons could be linked to other lasing NWs [61] (e.g. GaN and ZnO) and plasmonic NWs [62]. Notably, Sirbuly et al. [61] simultaneously guided the output of two (or more) nanolasers by coupling multiple ZnO and GaN wires to the same ribbon, establishing the possibility of performing all-NW nonlinear wave mixing within single nanocavities. In 2008, Park et al. [63] presented an optically or electrically driven photonic structure that used CdS NWs as photon sources to inject light into Si_3N_4 photonic-crystal waveguides. The photonic crystal was used to either guide or filter out different colors of light. In this work, the authors synthesized CdS/CdSe core/shell NWs consisting of two semiconductor materials, in which a CdS core emits green light and the CdSe shell emits red. By defining two photonic-crystal waveguides at either end, two different colors of light were sent in opposite directions. Later, Xu et al. [64] reported the design and realization of asymmetric light propagation in single CdS_xSe_{1-x} alloy NWs with a composition gradient along the length the NWs, as schematically shown in Fig. 6.6a. The bandgap of these NWs can be tuned from 2.4 eV at one end to 1.7 eV at the other end. Illumination of the entire NW showed that the PL color varied continuously from green to red along its length (Fig. 6.6b, c). In contrast to homogeneous NW

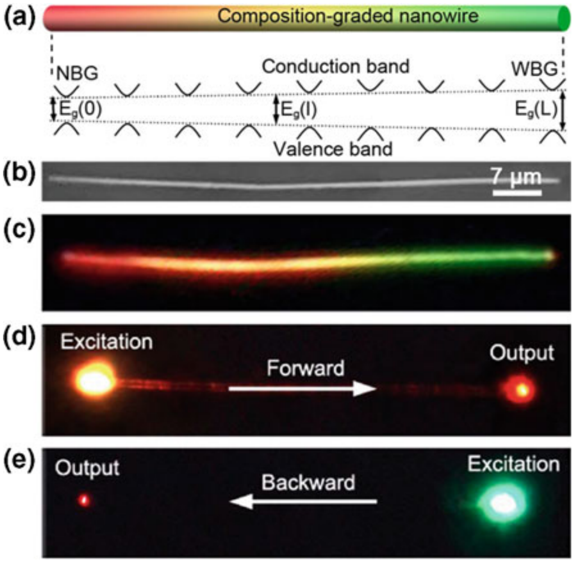

Fig. 6.6 **a** Schematic diagrams of a composition-graded NW and its corresponding bandgap structure. **b** SEM image of an examined composition-graded NW. **c** Real-color PL photograph of the NW under the illumination of a diffused 405-nm semiconductor laser. **d**, **e** Real-color PL photographs with local excitation at one of its ends. Reproduced from [64]. Copyright 2012 Nature Publishing Group

waveguides, light propagation along one axial direction of such composition-graded NWs is different to the propagation along the reverse direction, leading to asymmetric light propagation (Fig. 6.6d, e).

6.3.2 Nanoscale Light-Emitting Diodes

LED is a two-lead semiconductor light source that resembles a basic *p–n* junction diode, except that an LED also emits light [65]. In response to the passage of an electric current, electrons are able to recombine with holes within the device, releasing energy in the form of photons. The process is termed as electroluminescence (EL). In this section, we summarize recent advances in NW LED assembly, including crossed NW structures, axial and radial heterostructures, and branched NWs.

6.3.2.1 Crossed Nanowire Structures

Previously, we discussed the formation of NW *p–n* diodes by crossing a *p*- and a *n*-type NWs. In direct band gap semiconductors, the *p–n* diode also forms the basis for the critical optoelectronics devices, such as LEDs [14, 66, 67]. As an example, Huang et al. [14] fabricated nanoLEDs with colors spanning from the ultraviolet to near-infrared region of the electromagnetic spectrum. Single- and multicolor nanoLED devices and arrays are made with colors specified in a predictable way by

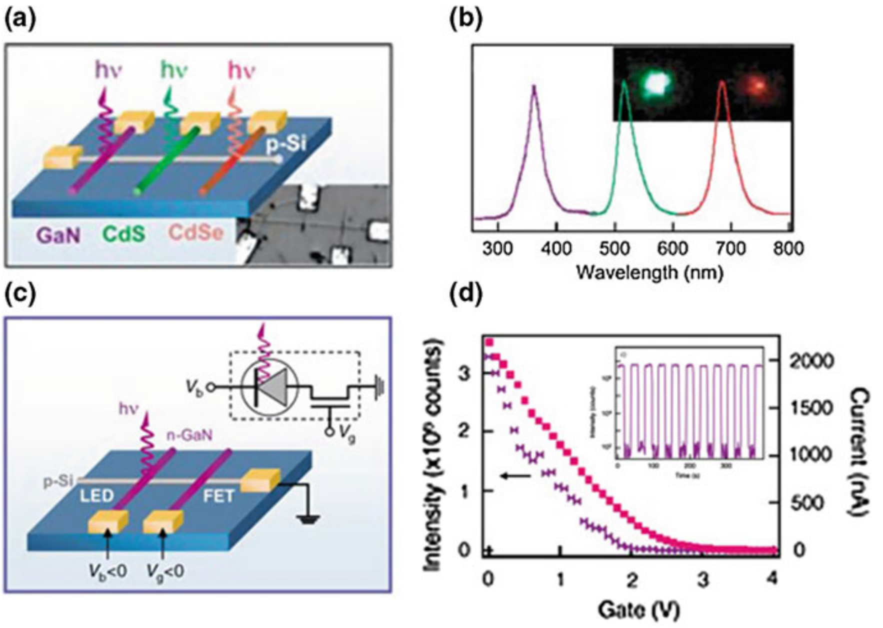

Fig. 6.7 **a** Schematic and corresponding SEM image of a tricolor nanoLED array. **b** Normalized EL spectra and color images from the three elements. **c** Schematic of an integrated crossed NW-FET and LED. **d** Plots of current and emission intensity of the nanoLED as a function of voltage applied to the NW gate at a fixed bias of −6 V. (*inset*) EL intensity versus time relation a voltage applied to NW gate is switched between 0 and +4 V for fixed bias of −6 V. Reproduced from [14]. Copyright 2005 John Wiley and Sons

the bandgaps of the III–V and II–VI NW building blocks. As shown in Fig. 6.7a, nanoLEDs with non-emissive SiNW hole-injectors are used to assemble multicolor arrays, in which *n*-type GaN, CdS, and CdSe NWs cross a single *p*-type SiNW. Normalized emission spectra recorded from the array demonstrates three spatially and spectrally distinct peaks with maxima at 365, 510, and 690 nm (Fig. 6.7b) consistent with band-edge emission from GaN, CdS, and CdSe, respectively. Color images of EL from the array show the green and red emission from *p*-Si/*n*-CdS and *p*-Si/*n*-CdSe crosses, respectively (inset, Fig. 6.7b). In addition, optoelectronic circuits consisting of integrated crossed NW LED and FET elements have been assembled (Fig. 6.7c). Specifically, one GaN NW forms a *p*–*n* diode with the SiNW, and a second GaN NW functions as a local gate, as described in the previous chapter. Measurements of current and emission intensity versus gate voltage showed that (i) the current decreased rapidly with increasing voltage as expected for a depletion mode FET, and (ii) the intensity of emitted light also decreased with increasing gate voltage. When the gate voltage was increased from 0 to +3 V, the current was reduced from ca. 2200 nA to an off state, where the supply voltage is −6 V (Fig. 6.7d). The ability to use the nanoscale FET to switch reversibly the nanoLED on and off has also been demonstrated (inset, Fig. 6.7d).

6.3.2.2 Axial Heterostructures

One of the first demonstrations of axial *p*–*n* junctions was made in vertical GaAs cone-like nanostructures grown epitaxially on GaAs(111)B substrates [68]. These structures also exhibited light emission by current injection at 77 K and room temperature. Later, the Lieber group [69] reported the synthesis of *n*-InP/*p*-InP modulation doped NWs and their applications as nanoscale LEDs. In a forward bias, individual InP NW devices exhibit light emission from *p*–*n* junctions, both highly polarized and blue-shifted due to the 1D structure and radial quantum confinement, respectively. Kim et al. [70] demonstrated the realization of the high-brightness and high-efficiency LEDs using dislocation-free InGaN/GaN MQW NW arrays. A blue-shift of EL occurs, directly with increasing current, which is attributed to screening of the built-in internal polarization field in the quantum wells by the injected carriers. Subsequently, Ra et al. [71] reported the controlled synthesis of InGaN/GaN MQW uniaxial (*c*-plane) and coaxial (*m*-plane) NW heterostructures. The *c*-plane and *m*-plane oriented MQW single NWs are utilized for the parallel assembly fabrication of the LEDs via a focused ion beam. The electrical properties of *m*-plane NWs exhibit superior characteristics than that of *c*-plane NWs, owing to the absence of piezoelectric polarization fields. Therefore, high-quality *m*-plane coaxial NWs can be utilized for the realization of high-brightness LEDs.

6.3.2.3 Radial Heterostructures

The radial NW concept also offers substantial opportunities for NW LEDs since the required *n*- and *p*-type active materials can be incorporated as the core and shell, enabling carrier injection or collection over a much larger area than those in crossed NW devices and axial NW heterostructures [33, 72, 73]. The Lieber group [33, 72] first demonstrated a general strategy for realizing these photonic nanostructures through the synthesis of well-defined doped III-nitride-based core-multishell (CMS) NW heterostructures (Fig. 6.8a). In these materials, a *n*-type GaN core and *p*-type GaN outer shell served as electron and hole injection layers, an $In_xGa_{1-x}N$ shell provided a tunable band gap quantum well for efficient radiative recombination of injected carriers, and an AlGaN shell was incorporated to enhance confinement of both carriers and photons in the InGaN active layer. Current versus voltage characteristics of CMS NW devices with separate contacts to the *n*-type core and *p*-type outer shell show the expected *p-n* diode current rectification (Fig. 6.8b). In a forward bias, the devices yield strong light emission with the LED color dependent on the indium composition in the CMS NW heterostructure that is defined during synthesis (Fig. 6.8c). Significantly, LED spectra collected from CMS NW devices with intentionally increasing indium composition demonstrate a systematic redshift of emission from 367 to 577 nm, covering the short wavelength region of the visible spectrum (Fig. 6.8d).

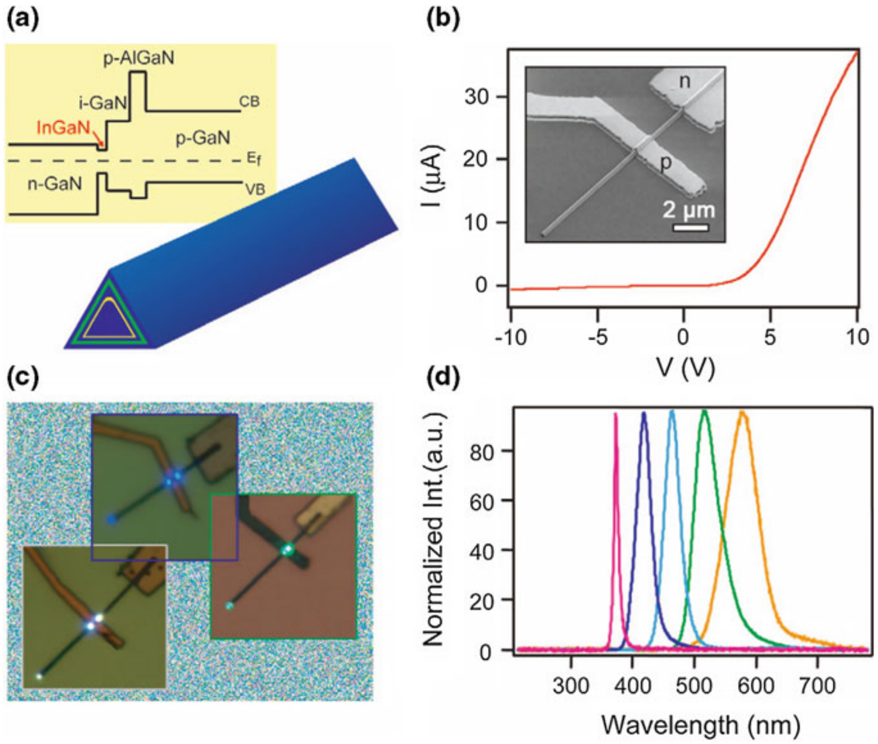

Fig. 6.8 **a** Schematic and corresponding band diagram for an *n*-GaN/InGaN/GaN/*p*-AlGaN/*p*-GaN CMS NW. The InGaN and AlGaN shells are highlighted with *yellow* and *green* colors, respectively. **b** *I-V* data recorded from a typical CMS NW device with contacts to the *n*-core and *p*-shell. **c** Electroluminescence (EL) images of three forward-biased CMS NW LEDs with ~15, 30, and 35 % In, showing *blue*, *greenish-blue*, and *greenish-yellow* emission, respectively. **d** Normalized EL spectra recorded from five multicolor CMS NW LEDs with 1, 10, 20, 25, and 35 % In (*left to right*), respectively. Reproduced from [72]. Copyright 2005 American Chemical Society

6.3.3 Optically-Pumped Nanowire Lasers

Semiconductor NWs with high optical gain offer promising solutions for lasers with small footprints and low power consumption. In this section, we introduce the principles of optically-pumped semiconductor NW lasers, followed by experimental demonstrations categorized by their output wavelengths within UV, visible, and near-IR spectral ranges, as well as multicolor emissions. For a comprehensive review of semiconductor NWs lasers, readers can refer to [11].

6.3.3.1 Principles of Optically-Pumped Nanowire Lasers

The word laser is an acronym for light amplification by stimulated emission of radiation. A laser is a device that is able to generate light via optical amplification based on the stimulated emission of electromagnetic radiation. Generally, three basic elements are necessary for a laser: an active gain medium that provides optical gain by stimulated emission, a pumping process to excite the electrons into higher energy levels to realize population inversion (i.e., the density of excited states is larger than that of the ground states), and an optical resonant cavity that confines the photons to create positive optical feedback [74]. In a stimulated emission, the probability of emission of a photon of a given frequency is enhanced by the presence of another photon of the same frequency. Therefore, stimulated emission induced by population inversion leads to an increase in the number of photons to produce a coherent beam. The realization of a semiconductor NW laser is similar to that of a bulk semiconductor lasers [11, 75]. The NWs can serve as both the gain medium, which is optically excited, and flat end facets can act as partially reflecting mirrors, which provide optical feedback as a Fabry-Perot cavity [76].

6.3.3.2 UV Lasers

Among semiconductor NW materials for lasing in the UV spectral range, ZnO and GaN have attracted the greatest research interest [77]. In this section, we introduce several experimental demonstrations of ZnO and GaN NW lasers. ZnO NWs have a bandgap of 3.37 eV, and a high exciton binding energy ($\sim$60 meV) that ensures efficient exciton emission above room temperature, making it an ideal candidate for UV lasing. The first NW laser was reported by the Yang group in 2001, where the room-temperature laser emission of ZnO NWs (with diameters varying from 20 to 150 nm and lengths up to 10 μm) was demonstrated [78]. Upon optical excitation, surface-emitting lasing was observed at 385 nm, with an emission line width less than 0.3 nm. Later, they also reported the first observation of single ZnO NWs acting as both optical waveguides and lasers, depending on the quality factor of the NW cavity [79]. In 2003, comb-like ZnO NW structures, with individual ZnO NWs (whose diameters range from 10 to 300 nm) evenly spaced on a stem with a regular periodicity of 0.1–2 μm, were constructed to be highly ordered NW ultraviolet laser arrays, in which each individual ZnO NW serves as a Fabry–Perot optical cavity [80]. Subsequently, Johnson et al. [81] utilized time-resolved second-harmonic generation (TRSHG) and transient PL spectroscopy to probe excited carriers immediately following band-gap excitation in single ZnO NW and nanoribbon lasers. They demonstrated transient PL consisting of a pump-independent slow component (free-exciton decay, 75–100 ps) and a significantly faster decay component that was correlated with stimulated emission (exciton-exciton lasing, $\sim$10 ps). Zhang et al. [82] measured the absolute light emission intensity, and both the external and internal quantum efficiency of ZnO NW nanolasers at room temperature. The external differential quantum efficiency reaches 60 % for lasing ZnO

NWs of 7.5 μm in length, compared to a value of approximately 10 % for PL. The absolute light emission intensity for individual NWs was found to be in the vicinity of 0.1 mW. By measuring the dependence of external differential quantum efficiency on the cavity length, the internal quantum efficiency was estimated to be about 85 %. Later, the influence of annealing on stimulated emission in ZnO nanorods was reported by Kwok et al. [83]. The lowest lasing threshold and defect emission as well as the longest spontaneous emission decay times were obtained for nanorods annealed in oxygen flow, which indicates that interstitial oxygen is not the dominant defect in hydrothermally grown nanorods. In 2008, Zimmler et al. [84] presented direct evidence of the transition from amplified spontaneous emission (ASE) to lasing in optically pumped ZnO NWs at room temperature. The optical power evolves from a superlinear region (characteristic of ASE) to a quasi-linear region (characteristic of laser oscillation) as the pump power exceeds threshold, concomitant with a transition to directional emission along the NW axis and the emergence of Fabry–Perot cavity modes around a wavelength of ~385 nm, the intensity of which exceeds the spontaneous emission background by orders of magnitude. In a later work, Gargas et al. [85] used pulsed laser spectroscopy and UV-confocal microscopy to characterize single vertical NW lasers. As shown in Fig. 6.9a, the PL spectra (vertically offset) are collected at pump energy densities of 383, 536, 980, 1378, 1454, and 1760 μJ/cm^2. The threshold in the 390 nm lasing spectra is estimated to be 400 μJ/cm^2. A 3D mapping of the PL emission intensity from a single vertical NW on a sapphire substrate is shown in Fig. 6.9b. The X and Y-axes denote spatial position, whereas the Z-axis represents the PL emission intensity collected at a set planar position.

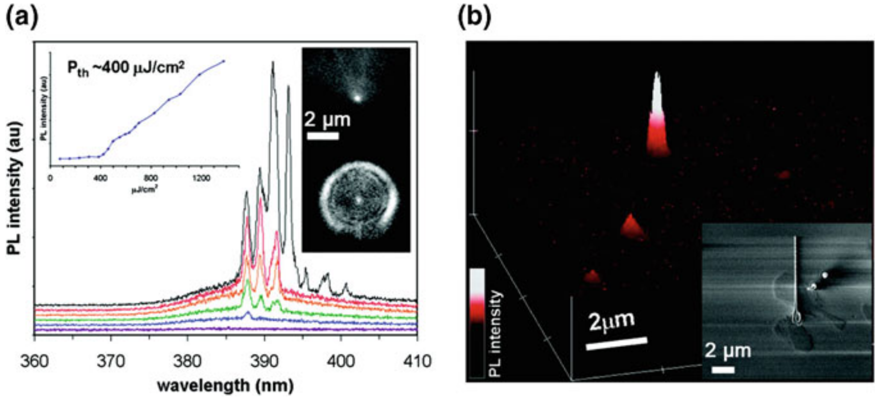

Fig. 6.9 **a** Diagram of a ZnO vertical NW cavity and its corresponding PL images collected along the NW. Lasing spectra of a single ZnO vertical NW cavity. *Left inset* power dependence graph showing lasing threshold at roughly 400 μJ/cm^2. *Right inset* dark-field images of a ZnO NW under white light illumination (*top*) and lasing induced by 266 nm pulsed excitation (*bottom*). **b** 3D confocal PL image of a ZnO vertical NW cavity. *Inset* SEM image of a ZnO vertical NW. Reproduced from [85]. Copyright 2009 American Chemical Society

The Wang group used the time-resolved PL to study three types of lasing mechanisms (i.e., exciton-exciton interaction, bipolaronic exciton condensation, and plasma) in pure, lightly doped, and heavily doped ZnO NWs [86]. Specifically, they demonstrated that the dopant concentration may significantly change the exciton-phonon coupling and the binding energy of excitons. Moreover, it may also affect the formation of bound excitons and exciton dissociation processes. Thus, all three types of lasing mechanisms can exist in ZnO NW lasers.

The UV-blue lasing behavior in single GaN NW was first observed in 2002 by Johnson et al. [87]. Lasing oscillation around 378 nm was observed in a 300 nm diameter and 40 μm long GaN NW, with evident axial Fabry–Perot cavity modes. Gradečak et al. [88] also studied GaN NWs with triangular cross sections, dislocation-free structures, and uniform diameters, which together contributed to excellent cavity properties, thus reducing the excitation power density (22 kW/cm^2) required for stimulated emission. Combining bottom-up and top-down approaches, Park et al. [89] constructed a GaN NW emitter with a fabricated Si_3N_4 stadium microresonator. The PL from the GaN NW was coupled and confined in the Si_3N_4 stadium microcavity. Using ultrafast optical pump-probe spectroscopy, Upadhya et al. [90] studied the influence of defect states on carrier dynamics in GaN NWs by probing carrier relaxation through the states responsible for yellow luminescence, an undesirable effect that plagues many GaN-based photonic devices [91, 92]. Lower growth temperature tends to allow more impurity sites in the NWs, which may trap photo-excited carriers and thus increase the lasing thresholds. Furthermore, excitation density-dependent measurements reveal a decrease in carrier lifetimes with increasing pump power. In 2014, Zhang et al. [93] demonstrated the first strong room temperature ultraviolet surface plasmon (SP) polariton laser with an extremely low threshold ($\sim$3.5 MW cm^{-2}). The authors found that a closed-contact planar semiconductor–insulator–metal interface greatly lessens the scattering loss, and efficiently promotes the exciton–SP energy transfer thus furnishes adequate optical gain to compensate the loss.

In addition to linear NW cavities, a ring-type cavity was formed by manipulating a GaN NW into a closed loop, and optically connecting both ends via evanescent coupling (Fig. 6.10a–c), which shows markedly different lasing and spontaneous emission properties compared to its linear counterpart. As shown in Fig. 6.10d, the laser-mode emission for the ring structure is substantially red-shifted relative to that for a linear cavity of similar length. This effect originates from enhanced coupling efficiencies for longer wavelengths across the overlapping junction, due to an increase of the electric field penetration depth with increasing wavelength [94].

6.3.3.3 Visible Lasers

CdS (2.42 eV) and CdSe NWs have been the most actively studied materials for lasing in the visible regime [11]. Detailed temperature-dependent optically-pumped studies of single CdS NW lasers reveal that a highly efficient exciton-exciton scattering phenomena was responsible for lasing from 4.2 to 70 K, when the lasing

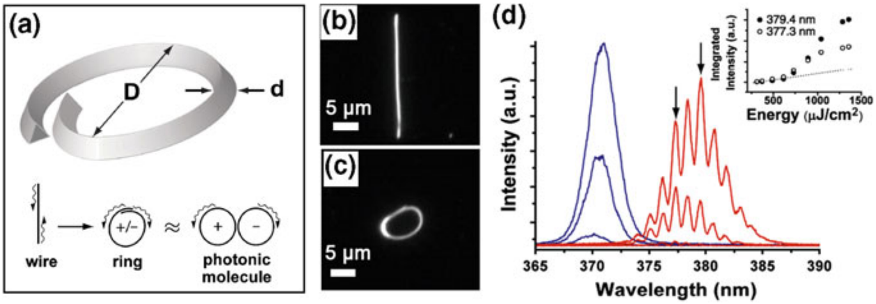

Fig. 6.10 **a** Schematic of ring and waveguiding analogy to coupled photonic molecule. **b**, **c** Dark-field images of a linear NW cavity and a ring-type NW cavity. **d** Comparison of lasing emission from ring and cavity geometries. *Inset* integrated area under ring modes, indicated by *arrows*. Reproduced from [94]. Copyright 2006 American Physical Society

mechanism shifts to an exciton-optic phonon scattering mechanism at higher temperatures [95]. In a later report [96], electric field modulation of visible NW laser consisting of single CdS NW was achieved using integrated, microfabricated electrodes. Modulation of laser emission intensity was achieved with no detectable change in the laser wavelength. The devices can also be operated below the lasing threshold to modulate the intensity of light propagating within the NW waveguide. As shown in Fig. 6.11a, electro-optic modulator (EOM) devices with a parallel-plate structure are used to apply a uniform electric field over a length *L* of the NW. Figure 6.11b shows the modulation of the output spectrum of a representative CdS NW EOM with modulation length (*L*) of 6 μm and SiO_2 dielectric thicknesses of 50 nm. The 489 nm lasing peak can be modulated by 40 % at 45 V, which is more than two times the modulation of the emission around 515 nm, while maintaining no detectable change in the laser wavelength (Fig. 6.11c). In 2011, Liu et al. [97] presented exciton-related optical studies of CdS nanobelts. The PL spectrum at 10 K shows rich spectral features identified by means of temperature-dependent spectral evolution. The strong excitonic emission in the samples enables the observation of random lasing action at room temperature. Geburt et al. [98] investigated the synthesis of various CdS nanostructures (bands, wires, irregular structures) and further investigated the lasing properties and necessary length-diameter relations for lasing of individual CdS NWs. Furthermore, CdSe NWs, with a bandgap of 1.74 eV, have also been used to realize red-color (around 710 nm wavelength) lasing [99, 100].

6.3.3.4 Near-IR Lasers

NW laser emission and waveguides with near-infrared (NIR) wavelengths are of interest given their potential suitability for applications in optical communications [11]. However, it has been challenging to obtain NIR NW lasers because a large

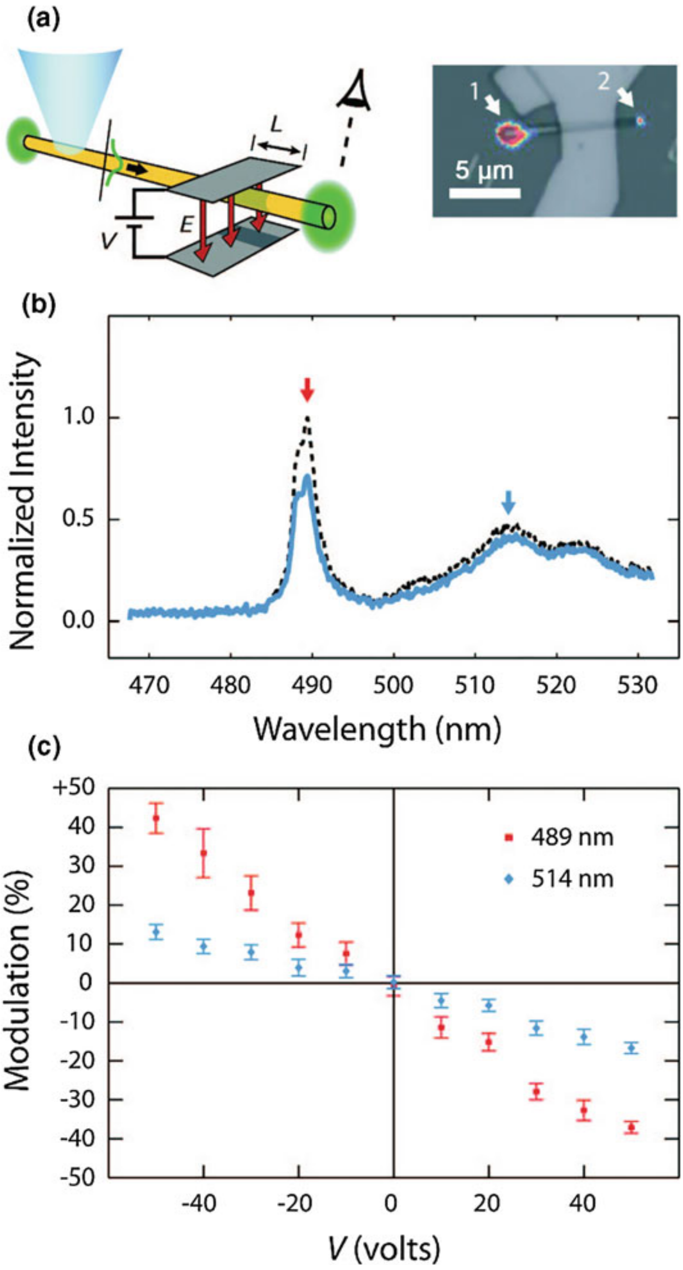

Fig. 6.11 **a** Diagram indicating the excitation site, region of field modulation, and observed NW end. At right, superimposed PL image (recorded below laser threshold) and white-light optical micrograph of a representative CdS NW EOM-laser device. Numerals 1 and 2 indicate excitation site and observed NW end, respectively. **b** Emission spectra of a CdS NW laser showing effect of a 30 V signal. **c** Modulation versus *V* at the two indicated wavelengths for the EOM-laser in (**b**). Reproduced from [96]. Copyright 2005 AIP Publishing LLC

fraction of the optical modes exist outside of the NWs for reasonable diameters, which increases propagation losses, and there is relatively poor reflectivity at the end facets. In 2006, Chin et al. [101] reported the first NIR NW lasing using subwavelength GaSb wires with a cross-sectional dimension of 700–1500 nm and lengths of 10–70 μm dispersed on a sapphire substrate. The measured lasing emission centered around 1553 nm. In the subsequent studies, the Fukui group also investigated GaAs, InP, and GaAs/GaAsP NIR NW lasers [102–104]. As an example, GaAs (1.424 eV) is an important NIR lasing material; however, a high density of surface states leads to strong decay of its emission quantum yield, making it difficult to realize GaAs NW lasers. In 2007, Hua et al. [102] investigated Fabry-Perot cavity effects in a single GaAs NW (320 nm in diameter, 4.5 μm in length), although the cavity losses were too large for lasing. After effectively passivating the surface states of a GaAs NW (290 nm in diameter, 2.8 μm in length) by a 50 nm GaAsP coating layer, the authors fabricated a high-quality optically active single GaAs/GaAsP coaxial core-shell NW, and realized 817 nm lasing under laser pulse excitation [104].

6.3.3.5 Wavelength-Tunable Lasers

In the previous sections, NW lasers for several homogeneous binary semiconductors have been discussed, where the lasing wavelengths correspond approximately to the fundamental bandgap energies of the respective homogeneous NW materials. The distinct NW bandgaps led to lasing over a relatively wide range of discrete wavelengths but did not enable continuous tuning in emission color. To address this issue, several research groups studied wavelength-tunable lasing in alloy systems. In 2005, Liu et al. [105] reported the first wavelength-controlled semiconductor NW lasers using ternary alloy $Zn_xCd_{1-x}S$ nanoribbons, which allows systematic variation of the bandgap of $Zn_xCd_{1-x}S$ from 2.42 eV for CdS to 3.7 eV for ZnS, and showed that it was possible to sustain lasing emission continuously in two spectral regions, 485–515 and 340–390 nm, by controlling the composition x close to CdS ($0.25 \geq x \geq 0$) and ZnS ($0.75 \geq x \geq 0$), respectively. Following this work, the synthesis of single crystal ternary CdS_xSe_{1-x} nanobelts and the observation of their color-tunable PL emission from green ($\sim$500 nm) to the near-infrared ($\sim$700 nm) was also demonstrated [106–110]. For example, by controlling local substrate temperature in a CVD system, Pan et al. [109] achieved spatial composition grading covering the complete composition range of ternary alloy CdSSe NWs on a single substrate of 1.2 cm in length. Figure 6.12a and b show real-color photographs of a quartz substrate with the as-grown NWs under regular room lighting (a) and under a 266 nm UV laser illumination (b), respectively. Figure 6.12c presents five SEM images taken from selected spots along the sample length, as indicated by the white spots in Fig. 6.12b. The as-grown sample shows the color change gradually from light-yellow (similar to CdS) to dark

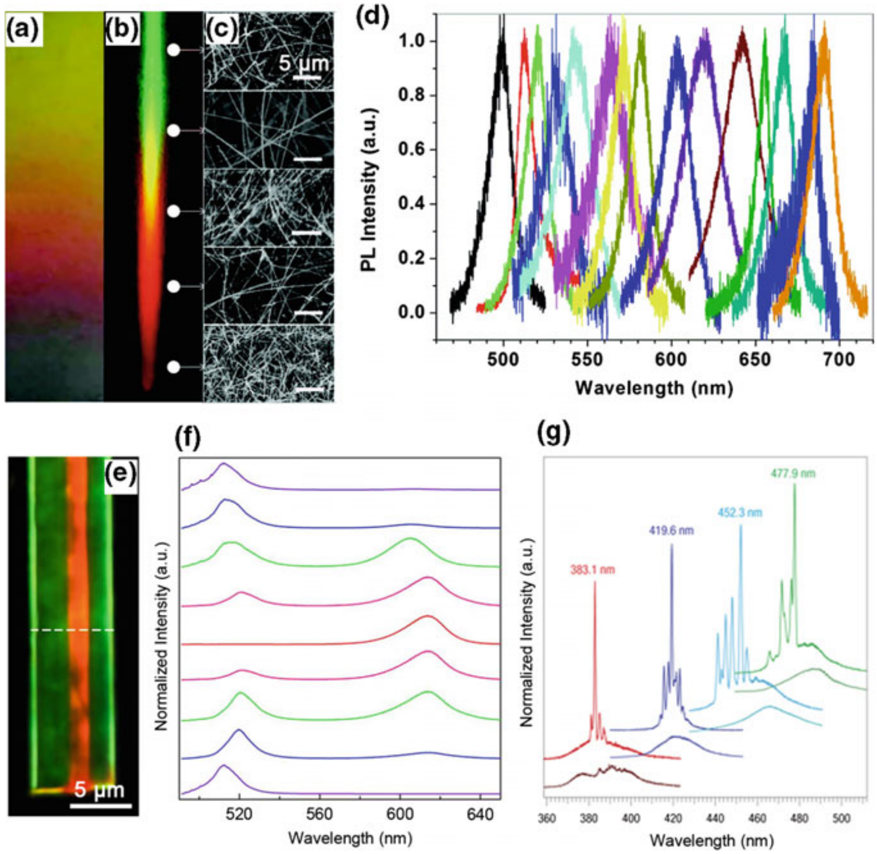

Fig. 6.12 **a**, **b** The real-color photographs of a quartz substrate with the as-grown spatially composition-graded CdSSe NWs under room lighting (**a**) and under UV laser illumination (**b**) (266 nm). Size of the substrate: 0.3 × 1.2 cm. **c** The SEM images taken at the white spots in panel **b**. **d** PL spectra collected at different locations along the substrate length. Reproduced from [109]. Copyright 2009 American Chemical Society. **e** A real-color photograph of a representative nanoribbon lateral heterostructure illuminated with a 405-nm laser. **f** PL spectra collected along the dashed line in (**e**). Reproduced from [113]. Copyright 2012 American Chemical Society. **g** PL spectra collected from four representative 26MQW NW structures with increasing In composition pumped at ~250 and ~700 kW cm^{-2}, respectively. Reproduced from [34]. Copyright 2008 Nature Publishing Group

(similar to CdSe) along the sample length direction, while the PL spectra exhibits the color change from green (consistent to the PL color of CdS) to red (consistent to the PL color of CdSe) along the same direction. These results indicate the formation of composition graded CdSSe alloys on a single substrate. Zapien et al. [111] and Luan et al. [112] have also shown that II–VI nanoribbons ($\text{CdS}_X\text{Se}_{1-X}$ and $\text{Zn}_Y\text{Cd}_{1-Y}\text{S}$) are capable of room-temperature lasing over the NIR to UV spectral range with CdS_xSe_{1-x} nanoribbons lasing from NIR (710 nm) to green (510 nm) as x changes from 0 to 1, and $Zn_YCd_{1-Y}S$ nanoribbons lasing from green (510 nm) to UV (340 nm) as Y varies from 0 to 1. In addition, Xu et al. [113] reported the growth of new CdS_xSe_{1-x}-CdS nanoribbon lateral heterostructures, with composition-tunable alloy CdS_xSe_{1-x} at the center and epitaxial CdS at the lateral sides. Under laser excitation, the emission of these ribbons indicates sandwich-like structures along the width direction, with characteristic red emission in the center and green emission at both edges (Fig. 6.12e, f). The spacing of the lasing wavelength of these nanoribbon lasers can be continuously tuned by controlling the composition and bandgap of the central CdS_xSe_{1-x} in the ribbons.

In previous examples of NW lasers, the NWs functioned as both the gain medium and optical cavity. However, Qian et al. [34] showed that decoupling the gain medium and cavity can offer advantages over homogeneous NW structures for designed laser wavelength output in parallel with independent optimization of the cavity. For example, they designed multi-quantum-well (MQW) NW structures composed of a GaN NW core, which functions as the primary part of the optical cavity, and epitaxial InGaN/GaN MQW shells, which serve as the composition-tunable gain medium. Optical excitation of individual MQW NW structures yield lasing with emission engineered from 365 to 494 nm through modulation of quantum well composition (Fig. 6.12g).

Recently, organic-inorganic perovskite material was introduced as a new system for NW lasers. Zhu et al. [114] studied room-temperature and wavelength-tunable lasing from single-crystal lead halide perovskite NWs with very low lasing thresholds (220 nJ cm^{-2}) and high quality factors ($Q \sim 3600$). The lasing threshold corresponds to a charge carrier density as low as 1.5×10^{16} cm^{-3}. Kinetic analysis based on time-resolved fluorescence revealed little charge carrier trapping in these single-crystal NWs and yielded estimated lasing quantum yields approaching 100 %.

6.3.3.6 Single-Mode Lasers

Semiconductor NW lasers usually exhibit multimode behaviors (i.e., emitting at multiple frequencies simultaneously) corresponding to the longitudinal modes of the NW Fabry–Perot cavities. In order to control the laser to oscillate at a single frequency, Xiao et al. [115] introduced an approach of coupling NW cavities by folding NWs into loop mirrors (LMs). According to the Vernier effect, when two sets of Fabry–Perot modes interact coherently with each other, only the modes that share the same frequencies will be observed in the lasing spectra. By having a single NW forming a small loop at one end, single frequency lasing with high suppression ratio (against the neighboring modes) around a wavelength of 738 nm was demonstrated in CdS NWs (Fig. 6.13). This form of wave coupling is highly sensitive to geometric parameters such as inter-NW distances, lengths of the coupled segments, and perimeters of the NW loops. Shortly after, the same group [116]

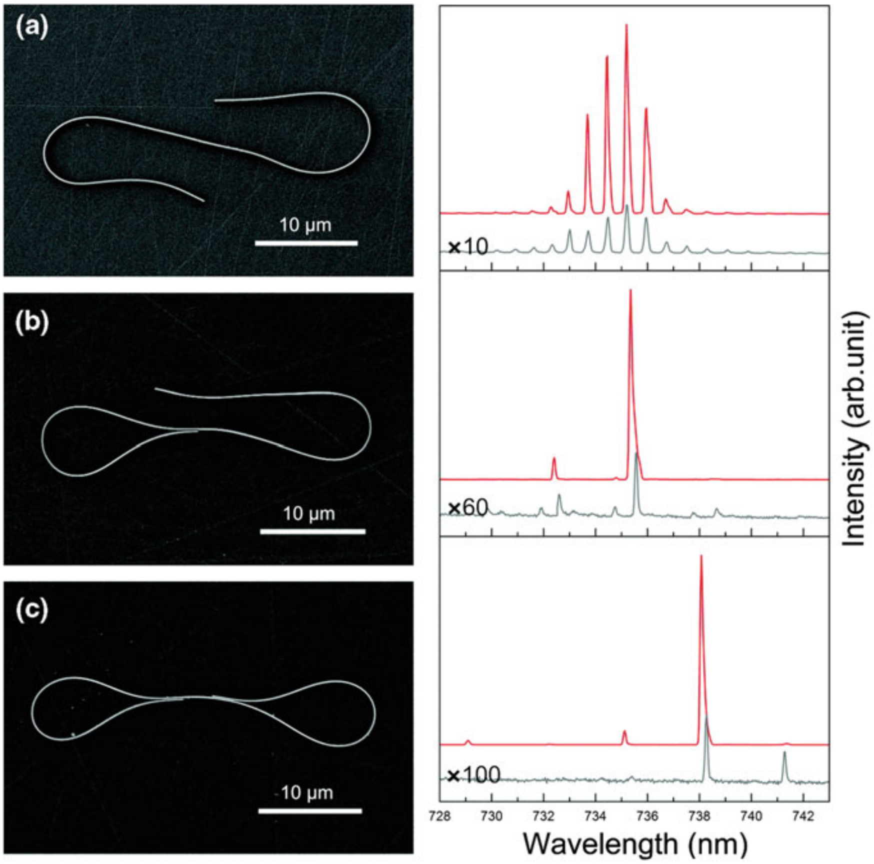

Fig. 6.13 SEM images and lasing spectra of single-NW structures **a** without LM, **b** with one LM, and **c** with double LMs. The *top lines* represent lasing spectra obtained at pump fluence well above the threshold, while the *bottom lines* represent the spectra obtained near the threshold. Reproduced from [115]. Copyright 2011 American Chemical Society

proposed another approach to enable single-mode lasing in coupled CdSe NW cavities, this is, coupling two CdSe NWs to form an X-structure coupled cavity for mode selection. Xu et al. [117] placed GaN NWs with different lengths side-by-side in contact to form a coupled cavity through nanoprobe manipulation. An alternative approach to achieve single-mode lasing is to construct two Fabry-Perot cavities that are axially coupled through an air gap [118]. The precisely defined smooth end-faces and inter-cavity gap widths (as narrow as 30 nm) on GaN NWs provide strong coupling between different cavities while maintaining low diffraction loss of the NWs. Single-wavelength lasing can be observed from the coupled cavity, and each component NW emits laser at multiple wavelengths when they are separated.

6.3.4 Electrically-Pumped Nanowire Lasers

Despite the excitement generated from the first demonstration of optically pumped NW lasers, it has been critical to achieve electrical injection NW lasers in terms of most technological applications. The first demonstration of electrically-pumped NW lasers was reported in 2003 [119]. To enable electrical injection of carriers in a NW optical cavity, *n*-CdS NWs were assembled on heavily doped *p*-Si substrates and contacts to CdS were fabricated by lithographic techniques (the *p*-Si substrate functioned as the second electrode), as shown schematically in Fig. 6.14a. A thin layer of Al_2O_3 is deposited in between the top and bottom contacts to force the current through the *p*-Si/*n*-CdS diode formed at the NW-substrate junction. The device under a low forward bias, produces EL with a broad featureless spectrum from the exposed NW end (Fig. 6.14b, c). Upon increasing the forward bias voltage or injection current, the electroluminescence spectrum quickly collapses into single mode lasing line at 493 nm with instrument resolution limited line-width of 0.7 nm, clearly demonstrating the possibility of electrically pumped lasing in NW optical cavities. In several other subsequent reports, ZnO NWs have been proved to be efficient electrically-pumped ultraviolet lasers [120–123]. For example, Chu et al. [121] demonstrated electrically pumped Fabry–Perot type waveguide lasing from laser diodes that consisted of Sb-doped *p*-type ZnO NWs and *n*-type ZnO thin films. By coating a MgO layer, which serves as electron blocking, hole supplying and surface passivation layer, electrically pumped near-ultraviolet lasing has been achieved in a metal/insulator/semiconductor (MIS) laser diode based on ZnO/MgO core/shell NWs [122]. Recently, the Mi group [124] reported the fabrication and performance of electrically driven lasers based on AlGaN core–shell NWs.

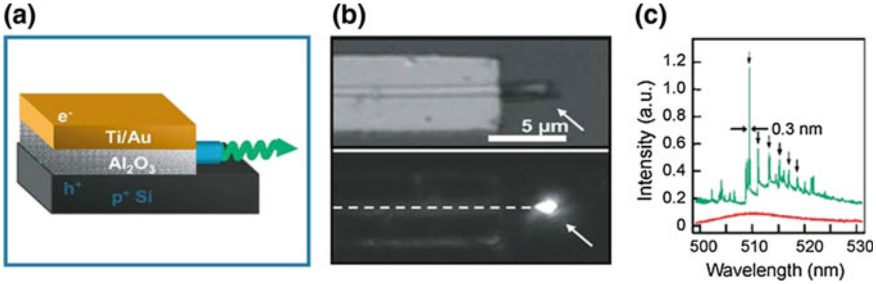

Fig. 6.14 **a** Schematic showing the NW electrical injection laser device structure. In this structure, electrons and holes can be injected into the CdS NW along the whole length from the top metal layer and the bottom *p*-Si layer, respectively. **b** *Top panel* shows an optical image of a laser device and the *arrow* highlights the exposed CdS NW end. *Bottom panel* shows an electroluminescence image recorded from this device. The *dashed line* highlights the NW position. **c** Electroluminescence spectra obtained from the NW end with injection currents of 120 µA (*red*, below lasing threshold) and 210 µA (*green*). The *black arrows* highlight F–P cavity modes with an average spacing of 1.83 nm. The *green* spectrum is shifted upwards by 0.15 intensity units for clarity. Reproduced from [119]. Copyright 2003 Nature Publishing Group (Color figure online)

These lasers emit across the entire ultraviolet AII band (320–340 nm) and work at a low temperature of 6 K. Because of the diffusion-driven compositions within the NWs, electrons and holes recombine more efficiently than usual.

6.3.5 Photodetectors

Photodetectors can sense incident photons, and are critical to many areas of science and technology [125]. Homogeneous NW photoconductors are the simplest configuration of NW-based photodetectors [18, 126]. The unique properties of individual NWs, such as light polarization sensitivity, light absorption enhancement, and internal photoconductive gain, can be exploited for the realization of efficient devices such as optical switches and interconnects, near-field imaging, and high-resolution detectors. Apart from NW photoconductors, other one-dimensional photodetector structures based on semiconducting or superconducting NWs are being actively investigated for efficient conversion of optical to electrical signals. In this section, we present NW photodetector concepts demonstrated in previous literature, including photodiodes, phototransistors, and detectors based on superconducting NWs. Several comprehensive reviews about NW photodetectors can be found in [127].

6.3.5.1 Photodiodes

Photodetection has been realized in diodes consisting of homo- and heterogeneous semiconductor NW junctions, either formed within single NWs during growth or as crossed NW configurations [128–132]. In the case of the *n*-CdS/*p*-Si crossed avalanche photodiode, a photocurrent increase ($I_{\mathrm{PC}}/I_{\mathrm{dark}}$) of ~10,000 times higher than in individual *n*-CdS or *p*-SiNW photoconductors has been observed, due to avalanche multiplication at the *p*-*n* crossed NW junction, with multiplication factors as high as $M = 7 \times 10^4$. It has been demonstrated that the NW avalanche photodiodes (APDs) have ultrahigh sensitivity with detection limits of less than 100 photons, and subwavelength spatial resolution of at least 250 nm [131]. Later, the same group [132] obtained similar sensitivity in the case of the axial *p*-*i*-*n* SiNW avalanche photodiodes, with multiplication factors in excess of ca. 30. Interestingly, electron- and hole-initiated avalanche gains are separately measured by localized photoexcitation of the *p*-type and *n*-type regions, yielding multiplication factors of ca. 100 and 20, respectively. Furthermore, metal-semiconductor junctions (i.e., Schottky junctions) [133–135] can also be used as photodiodes, where the electrons excited in the metal and the electron–hole pairs generated in the semiconductor can both contribute to the photocurrent. As an example, Gu et al. [134] reported the application of a near-field scanning optical microscope (NSOM) to map the local photocurrent in individual CdS NWs configured as metal-semiconductor-metal (MSM) photodetectors. The NW MSM photodetectors exhibited photocurrents $\sim 10^5$ larger than the dark current under uniform monochromatic illumination. Under local illumination, the photoresponse was localized to the near-contact regions.

6.3.5.2 Phototransistors

A phototransistor is a bipolar or unipolar transistor where light can reach the base, creating optically generated carriers. Upon illumination, the base-collector junction can be modulated, resulting in an amplified current, which can lead to much greater photosensitivity. In 2002, Fujiwara et al. [136] demonstrated the detection of single electrons and single holes in SiNW transistors using an electron-hole system. Photogenerated carriers were stored in a quantum dot electrically formed in a SiNW by a front gate. The stored charges affected the current of the complementary carriers that flow along the bottom of the SiNW. A linear photoresponce of single-charge generation was observed. Later, the Park group [133, 137] reported both Si and Ge NW-FETs as polarization-sensitive, high-resolution light detectors in the visible range.

6.3.5.3 Superconductor Nanowire Photodetectors

Another photodetetector concept that makes use of the unique geometrical properties of NWs is that of superconducting NW photodetectors, which are able to perform single-photon counting with exceptional sensitivity and time resolution at near-infrared wavelengths. Demonstrations of this concept have focused on NbN NWs with typical dimensions of $\sim$ 5 nm thickness and 50–200 nm width [138–143]. The working principle of superconducting NW detectors is described as follows [144]: the NW is maintained well below its superconducting critical temperature, T_c, and direct current biased just below its critical current. The absorption of a photon with energy higher than the superconducting energy gap creates a local nonequilibrium perturbation with a large number of excited hot electrons, which increases the average electron temperature above T_c and results in the formation of a hotspot—a local nonsuperconducting region. The local current density in the sidewalks increases beyond the critical current density and forms a resistive barrier across the width of the NW. The sudden increase in resistance from zero to a finite value generates a measurable output voltage pulse across the NW.

6.4 Future Directions and Challenges

Chemically synthesized NWs have witnessed a substantial interest in the past decade for building up photonic devices, and have been demonstrated for a host of photonic building blocks that exhibit sub-wavelength optical functionalities, such as light emission, lasing, waveguiding and nonlinear optical mixing. Nonetheless, enormous challenges still remain to realize arrays of devices and circuits from these unique NW materials.

First, it is still challenging to achieve the accurate control of NW growth, including geometric perfection, size dispersion, and shape control, which are critical for developing high quality photonic devices due to, for example, changes in light confinements in these subwavelength structures. Second, although the 1D nanosized feature of NWs is appealing for high optical quality, these NWs have a significant external surface area, which potentially introduces a high density of surface-trap states that reduce desired radiative quantum yields (i.e., emission efficiency). Thus, proper passivation of those surface states should be considered to optimize the NW-based solid-state lighting. Third, compared to monolithic structures defined by lithography the efficiency of light coupling between adjacent NWs has been low. A potential approach to improve this coupling efficiency will be to grow branched NW structures with clean and crystalline interfaces. Fourth, quantitative and critical comparisons between NW photonic structures and conventional thin-film technologies, in terms of efficiency, fabrication cost and stability, is still lacking. Such benchmarking is important to evaluate whether this new class of nanostructures is a viable candidate for future generation of photonic technologies as commonly proposed, or perhaps, a new direction not yet envisioned where the unique properties can be better exploited. We suggest this avenue of thought and investigation, for example taking advantage of unique size and assembly capabilities to make very nontraditional free standing and three-dimensional structures, may yield the most impact in the future perhaps at the interface between nanophotonics, nanoelectronics and biology.

References

1. A. Yariv, P. Yeh, *Photonics: Optical Electronics in Modern Communications (The Oxford Series in Electrical and Computer Engineering)* (Oxford University Press Inc., New York, 2006)
2. M.J. Deen, P.K. Basu, *Silicon Photonics: Fundamentals and Devices* (Wiley, Chichester, 2012)
3. R.G. Hobbs, N. Petkov, J.D. Holmes, Semiconductor nanowire fabrication by bottom-up and top-down paradigms. Chem. Mat. **24**(11), 1975–1991 (2012)
4. C.M. Lieber, Nanoscale science and technology: building a big future from small things. MRS Bull. **28**(07), 486–491 (2003)
5. C.M. Lieber, Z.L. Wang, Functional nanowires. MRS Bull. **32**(02), 99–108 (2007)
6. C.M. Lieber, Semiconductor nanowires: a platform for nanoscience and nanotechnology. MRS Bull. **36**(12), 1052–1063 (2011)
7. Y.-Z. Long, M. Yu, B. Sun, C.-Z. Gu, Z. Fan, Recent advances in large-scale assembly of semiconducting inorganic nanowires and nanofibers for electronics, sensors and photovoltaics. Chem. Soc. Rev. **41**(12), 4560–4580 (2012)
8. R. Agarwal, C.M. Lieber, Semiconductor nanowires: optics and optoelectronics. Appl. Phys. A **85**(3), 209–215 (2006)

9. Y. Li, F. Qian, J. Xiang, C.M. Lieber, Nanowire electronic and optoelectronic devices. Mater. Today **9**(10), 18–27 (2006)
10. D.J. Sirbuly, M. Law, H. Yan, P. Yang, Semiconductor nanowires for subwavelength photonics integration. J. Phys. Chem. B **109**(32), 15190–15213 (2005)
11. Y. Ma, X. Guo, X. Wu, L. Dai, L. Tong, Semiconductor nanowire lasers. Adv. Opt. Photonics **5**(3), 216–273 (2013)
12. P.J. Pauzauskie, P. Yang, Nanowire photonics. Mater. Today **9**(10), 36–45 (2006)
13. R. Yan, D. Gargas, P. Yang, Nanowire photonics. Nat. Photonics **3**(10), 569–576 (2009)
14. Y. Huang, X. Duan, C.M. Lieber, Nanowires for integrated multicolor nanophotonics. Small **1**(1), 142–147 (2005)
15. K. Hiruma, M. Yazawa, T. Katsuyama, K. Ogawa, K. Haraguchi, M. Koguchi, H. Kakibayashi, Growth and optical properties of nanometer-scale GaAs and InAs whiskers. J. Appl. Phys. **77**(2), 447–462 (1995)
16. Y. Nagamune, H. Watabe, F. Sogawa, Y. Arakawa, One-dimensional exciton diffusion in GaAs quantum wires. Appl. Phys. Lett. **67**(11), 1535–1537 (1995)
17. X. Duan, J. Wang, C.M. Lieber, Synthesis and optical properties of gallium arsenide nanowires. Appl. Phys. Lett. **76**(9), 1116–1118 (2000)
18. J. Wang, M.S. Gudiksen, X. Duan, Y. Cui, C.M. Lieber, Highly polarized photoluminescence and photodetection from single indium phosphide nanowires. Science **293**(5534), 1455–1457 (2001)
19. M.S. Gudiksen, J. Wang, C.M. Lieber, Size-dependent photoluminescence from single indium phosphide nanowires. J. Phys. Chem. B **106**(16), 4036–4039 (2002)
20. H.W. Seo, S.Y. Bae, J. Park, H. Yang, K.S. Park, S. Kim, Strained gallium nitride nanowires. J. Chem. Phys. **116**(21), 9492–9499 (2002)
21. P. Yang, H. Yan, S. Mao, R. Russo, J. Johnson, R. Saykally, N. Morris, J. Pham, R. He, H.-J. Choi, Controlled growth of ZnO nanowires and their optical properties. Adv. Funct. Mater. **12**(5), 323 (2002)
22. Q. Xiong, G. Chen, J. Acord, X. Liu, J. Zengel, H. Gutierrez, J. Redwing, L. Lew Yan Voon, B. Lassen, P. Eklund, Optical properties of rectangular cross-sectional ZnS nanowires. Nano Lett. **4**(9), 1663–1668 (2004)
23. B. Xiang, H. Zhang, G. Li, F. Yang, F. Su, R. Wang, J. Xu, G. Lu, X. Sun, Q. Zhao, Green-light-emitting ZnSe nanowires fabricated via vapor phase growth. Appl. Phys. Lett. **82** (19), 3330–3332 (2003)
24. P.V. Radovanovic, C.J. Barrelet, S. Gradecak, F. Qian, C.M. Lieber, General synthesis of manganese-doped II-VI and III-V semiconductor nanowires. Nano Lett. **5**(7), 1407–1411 (2005)
25. C. Ma, Y. Ding, D. Moore, X. Wang, Z.L. Wang, Single-crystal CdSe nanosaws. J. Am. Chem. Soc. **126**(3), 708–709 (2004)
26. S. Bhattacharya, D. Banerjee, K. Adu, S. Samui, S. Bhattacharyya, Confinement in silicon nanowires: optical properties. Appl. Phys. Lett. **85**(11), 2008–2010 (2004)
27. D. van Dam, D.R. Abujetas, R. Paniagua-Dominguez, J.A. Sánchez-Gil, E.P. Bakkers, J. Haverkort, J. Gómez-Rivas, Directional and polarized emission from nanowire arrays. Nano Lett. **15**(7), 4557–4563 (2015)
28. R. Solanki, J. Huo, J. Freeouf, B. Miner, Atomic layer deposition of ZnSe/CdSe superlattice nanowires. Appl. Phys. Lett. **81**(20), 3864–3866 (2002)
29. W.I. Park, G.C. Yi, M. Kim, S.J. Pennycook, Quantum confinement observed in ZnO/ZnMgO nanorod heterostructures. Adv. Mater. **15**(6), 526–529 (2003)
30. N. Panev, A.I. Persson, N. Sköld, L. Samuelson, Sharp exciton emission from single InAs quantum dots in GaAs nanowires. Appl. Phys. Lett. **83**(11), 2238–2240 (2003)
31. P. Poole, J. Lefebvre, J. Fraser, Spatially controlled, nanoparticle-free growth of InP nanowires. Appl. Phys. Lett. **83**(10), 2055–2057 (2003)
32. M.J. Holmes, K. Choi, S. Kako, M. Arita, Y. Arakawa, Room-temperature triggered single photon emission from a III-nitride site-controlled nanowire quantum dot. Nano Lett. **14**(2), 982–986 (2014)

33. F. Qian, Y. Li, S. Gradecak, D. Wang, C.J. Barrelet, C.M. Lieber, Gallium nitride-based nanowire radial heterostructures for nanophotonics. Nano Lett. **4**(10), 1975–1979 (2004)
34. F. Qian, Y. Li, S. Gradečak, H.-G. Park, Y. Dong, Y. Ding, Z.L. Wang, C.M. Lieber, Multi-quantum-well nanowire heterostructures for wavelength-controlled lasers. Nat. Mater. **7**(9), 701–706 (2008)
35. F. Qian, M. Brewster, S.K. Lim, Y. Ling, C. Greene, O. Laboutin, J.W. Johnson, S. Gradečak, Y. Cao, Y. Li, Controlled synthesis of AlN/GaN multiple quantum well nanowire structures and their optical properties. Nano Lett. **12**(6), 3344–3350 (2012)
36. Y.-R. Shen, *Principles of Nonlinear Optics* (Wiley, New York, 1984)
37. R.W. Boyd, *Nonlinear Optics*, 2nd edn. (Academic Press, San Diego, 2003)
38. S. Yue, M.N. Slipchenko, J.X. Cheng, Multimodal nonlinear optical microscopy. Laser Photonics Rev. **5**(4), 496–512 (2011)
39. L. Tong, J.-X. Cheng, Label-free imaging through nonlinear optical signals. Mater. Today **14** (6), 264–273 (2011)
40. R. Cisek, V. Barzda, H.E. Ruda, A. Shik, Nonlinear optical properties of semiconductor nanowires. IEEE J. Sel. Top. Quant. **17**(4), 915–921 (2011)
41. C.J. Barrelet, H.-S. Ee, S.-H. Kwon, H.-G. Park, Nonlinear mixing in nanowire subwavelength waveguides. Nano Lett. **11**(7), 3022–3025 (2011)
42. J.C. Johnson, H. Yan, R.D. Schaller, P.B. Petersen, P. Yang, R.J. Saykally, Near-field imaging of nonlinear optical mixing in single zinc oxide nanowires. Nano Lett. **2**(4), 279–283 (2002)
43. J. Long, B. Simpkins, D. Rowenhorst, P. Pehrsson, Far-field imaging of optical second-harmonic generation in single GaN nanowires. Nano Lett. **7**(3), 831–836 (2007)
44. Y. Nakayama, P.J. Pauzauskie, A. Radenovic, R.M. Onorato, R.J. Saykally, J. Liphardt, P. Yang, Tunable nanowire nonlinear optical probe. Nature **447**(7148), 1098–1101 (2007)
45. F. Wang, P.J. Reece, S. Paiman, Q. Gao, H.H. Tan, C. Jagadish, Nonlinear optical processes in optically trapped InP nanowires. Nano Lett. **11**(10), 4149–4153 (2011)
46. R. Sanatinia, M. Swillo, S. Anand, Surface second-harmonic generation from vertical GaP nanopillars. Nano Lett. **12**(2), 820–826 (2012)
47. X. Liu, Q. Zhang, W.K. Chong, J.N. Yip, X. Wen, Z. Li, F. Wei, G. Yu, Q. Xiong, T.C. Sum, Cooperative enhancement of second-harmonic generation from a single CdS nanobelt-hybrid plasmonic structure. ACS Nano **9**(5), 5018–5026 (2015)
48. R. Sanatinia, S. Anand, M. Swillo, Modal engineering of second-harmonic generation in single GaP nanopillars. Nano Lett. **14**(9), 5376–5381 (2014)
49. O. Schwartz, D. Oron, Background-free third harmonic imaging of gold nanorods. Nano Lett. **9**(12), 4093–4097 (2009)
50. Y. Jung, L. Tong, A. Tanaudommongkon, J.-X. Cheng, C. Yang, In vitro and in vivo nonlinear optical imaging of silicon nanowires. Nano Lett. **9**(6), 2440–2444 (2009)
51. J. Jang, S. Park, N. Frazer, J. Ketterson, S. Lee, B. Roy, J. Cho, Strong P-band emission and third harmonic generation from ZnO nanorods. Solid State Commun. **152**(14), 1241–1243 (2012)
52. Y. Jung, H. Chen, L. Tong, J.-X. Cheng, Imaging gold nanorods by plasmon-resonance-enhanced four wave mixing. J. Phys. Chem. C **113**(7), 2657–2663 (2009)
53. E. Poutrina, C. Ciracì, D.J. Gauthier, D.R. Smith, Enhancing four-wave-mixing processes by nanowire arrays coupled to a gold film. Opt. Express **20**(10), 11005–11013 (2012)
54. Y. Wang, C.-Y. Lin, A. Nikolaenko, V. Raghunathan, E.O. Potma, Four-wave mixing microscopy of nanostructures. Adv. Opt. Photonics **3**(1), 1–52 (2011)
55. R.W. Hellwarth, Theory of stimulated Raman scattering. Phys. Rev. **130**(5), 1850 (1963)
56. M.F.S. Ferreira, Stimulated Raman scattering. In *Nonlinear Effects in Optical Fibers* (Wiley, New Jersey, 2011), pp. 245–272
57. J. Wu, A.K. Gupta, H.R. Gutierrez, P.C. Eklund, Cavity-enhanced stimulated Raman scattering from short GaP nanowires. Nano Lett. **9**(9), 3252–3257 (2009)

58. L. Tong, R.R. Gattass, J.B. Ashcom, S. He, J. Lou, M. Shen, I. Maxwell, E. Mazur, Subwavelength-diameter silica wires for low-loss optical wave guiding. Nature **426**(6968), 816–819 (2003)
59. C.J. Barrelet, A.B. Greytak, C.M. Lieber, Nanowire photonic circuit elements. Nano Lett. **4** (10), 1981–1985 (2004)
60. M. Law, D.J. Sirbuly, J.C. Johnson, J. Goldberger, R.J. Saykally, P. Yang, Nanoribbon waveguides for subwavelength photonics integration. Science **305**(5688), 1269–1273 (2004)
61. D.J. Sirbuly, M. Law, P. Pauzauskie, H. Yan, A.V. Maslov, K. Knutsen, C.-Z. Ning, R. J. Saykally, P. Yang, Optical routing and sensing with nanowire assemblies. Proc. Natl. Acad. Sci. U.S.A. **102**(22), 7800–7805 (2005)
62. R. Yan, P. Pausauskie, J. Huang, P. Yang, Direct photonic–plasmonic coupling and routing in single nanowires. Proc. Natl. Acad. Sci. U.S.A. **106**(50), 21045–21050 (2009)
63. H.-G. Park, C.J. Barrelet, Y. Wu, B. Tian, F. Qian, C.M. Lieber, A wavelength-selective photonic-crystal waveguide coupled to a nanowire light source. Nat. Photonics **2**(10), 622–626 (2008)
64. J. Xu, X. Zhuang, P. Guo, W. Huang, W. Hu, Q. Zhang, Q. Wan, X. Zhu, Z. Yang, L. Tong, Asymmetric light propagation in composition-graded semiconductor nanowires. Sci. Rep. **2**, 820 (2012)
65. E.F. Schubert, J. Cho, J.K. Kim, Light-emitting diodes. In *Kirk-Othmer Encyclopedia of Chemical Technology* (Wiley, Hoboken, NJ, 2015)
66. X. Duan, Y. Huang, Y. Cui, J. Wang, C.M. Lieber, Indium phosphide nanowires as building blocks for nanoscale electronic and optoelectronic devices. Nature **409**(6816), 66–69 (2001)
67. Z. Zhong, F. Qian, D. Wang, C.M. Lieber, Synthesis of p-type gallium nitride nanowires for electronic and photonic nanodevices. Nano Lett. **3**(3), 343–346 (2003)
68. K. Haraguchi, T. Katsuyama, K. Hiruma, K. Ogawa, GaAs p-n junction formed in quantum wire crystals. Appl. Phys. Lett. **60**(6), 745–747 (1992)
69. M.S. Gudiksen, L.J. Lauhon, J. Wang, D.C. Smith, C.M. Lieber, Growth of nanowire superlattice structures for nanoscale photonics and electronics. Nature **415**(6872), 617–620 (2002)
70. H.-M. Kim, Y.-H. Cho, H. Lee, S.I. Kim, S.R. Ryu, D.Y. Kim, T.W. Kang, K.S. Chung, High-brightness light emitting diodes using dislocation-free indium gallium nitride/gallium nitride multiquantum-well nanorod arrays. Nano Lett. **4**(6), 1059–1062 (2004)
71. Y.-H. Ra, R. Navamathavan, H.-I. Yoo, C.-R. Lee, Single Nanowire Light-Emitting Diodes Using Uniaxial and Coaxial InGaN/GaN Multiple Quantum Wells Synthesized by Metalorganic Chemical Vapor Deposition. Nano Lett. **14**, 1537–1545 (2014)
72. F. Qian, S. Gradecak, Y. Li, C.-Y. Wen, C.M. Lieber, Core/multishell nanowire heterostructures as multicolor, high-efficiency light-emitting diodes. Nano Lett. **5**(11), 2287–2291 (2005)
73. Y.-H. Ra, R. Navamathavan, J.-H. Park, C.-R. Lee, Coaxial $In_xGa_{1-x}N$/GaN multiple quantum well nanowire arrays on Si(111) substrate for high-performance light-emitting diodes. Nano Lett. **13**(8), 3506–3516 (2013)
74. O. Svelto, D.C. Hanna, *Principles of Lasers*, 5th edn. (Springer, New York, 2010)
75. M.A. Zimmler, F. Capasso, S. Müller, C. Ronning, Optically pumped nanowire lasers: invited review. Semicond. Sci. Tech. **25**(2), 024001 (2010)
76. R.M. Ma, R.F. Oulton, V.J. Sorger, X. Zhang, Plasmon lasers: coherent light source at molecular scales. Laser Photonics Rev. **7**(1), 1–21 (2013)
77. D. Vanmaekelbergh, L.K. van Vugt, ZnO nanowire lasers. Nanoscale **3**(7), 2783–2800 (2011)
78. M.H. Huang, S. Mao, H. Feick, H. Yan, Y. Wu, H. Kind, E. Weber, R. Russo, P. Yang, Room-temperature ultraviolet nanowire nanolasers. Science **292**(5523), 1897–1899 (2001)
79. J.C. Johnson, H. Yan, R.D. Schaller, L.H. Haber, R.J. Saykally, P. Yang, Single nanowire lasers. J. Phys. Chem. B **105**(46), 11387–11390 (2001)
80. H. Yan, R. He, J. Johnson, M. Law, R.J. Saykally, P. Yang, Dendritic nanowire ultraviolet laser array. J. Am. Chem. Soc. **125**(16), 4728–4729 (2003)

81. J.C. Johnson, K.P. Knutsen, H. Yan, M. Law, Y. Zhang, P. Yang, R.J. Saykally, Ultrafast carrier dynamics in single ZnO nanowire and nanoribbon lasers. Nano Lett. **4**(2), 197–204 (2004)
82. Y. Zhang, R.E. Russo, S.S. Mao, Quantum efficiency of ZnO nanowire nanolasers. Appl. Phys. Lett. **87**(4), 043106–043106–3 (2005)
83. W. Kwok, A.B. Djurišić, Y.H. Leung, D. Li, K. Tam, D. Phillips, W. Chan, Influence of annealing on stimulated emission in ZnO nanorods. Appl. Phys. Lett. **89**(18), 183112 (2006)
84. M.A. Zimmler, J. Bao, F. Capasso, S. Müller, C. Ronning, Laser action in nanowires: observation of the transition from amplified spontaneous emission to laser oscillation. Appl. Phys. Lett. **93**(5), 051101 (2008)
85. D.J. Gargas, M.E. Toimil-Molares, P. Yang, Imaging single ZnO vertical nanowire laser cavities using UV-laser scanning confocal microscopy. J. Am. Chem. Soc. **131**(6), 2125–2127 (2009)
86. B. Zou, R. Liu, F. Wang, A. Pan, L. Cao, Z.L. Wang, Lasing mechanism of ZnO nanowires/nanobelts at room temperature. J. Phys. Chem. B **110**(26), 12865–12873 (2006)
87. J.C. Johnson, H.-J. Choi, K.P. Knutsen, R.D. Schaller, P. Yang, R.J. Saykally, Single gallium nitride nanowire lasers. Nat. Mater. **1**(2), 106–110 (2002)
88. S. Gradečak, F. Qian, Y. Li, H.-G. Park, C.M. Lieber, GaN nanowire lasers with low lasing thresholds. Appl. Phys. Lett. **87**(17), 173111 (2005)
89. H.-G. Park, F. Qian, C.J. Barrelet, Y. Li, Microstadium single-nanowire laser. Appl. Phys. Lett. **91**(25), 251115–251115-3 (2007)
90. P.C. Upadhya, Q. Li, G.T. Wang, A.J. Fischer, A.J. Taylor, R.P. Prasankumar, The influence of defect states on non-equilibrium carrier dynamics in GaN nanowires. Semicond. Sci. Tech. **25**(2), 024017 (2010)
91. A. Armstrong, Q. Li, K.H.A. Bogart, Y. Lin, G.T. Wang, A.A. Talin, Deep level optical spectroscopy of GaN nanorods. J. Appl. Phys. **106**(5), 053712 (2009)
92. A. Armstrong, G. Wang, A. Talin, Depletion-mode photoconductivity study of deep levels in GaN nanowires. J. Electron. Mater. **38**(4), 484–489 (2009)
93. Q. Zhang, G. Li, X. Liu, F. Qian, Y. Li, T.C. Sum, C.M. Lieber, Q. Xiong, A room temperature low-threshold ultraviolet plasmonic nanolaser. Nat. Commun. **5**, 4953 (2014)
94. P.J. Pauzauskie, D.J. Sirbuly, P. Yang, Semiconductor nanowire ring resonator laser. Phys. Rev. Lett. **96**(14), 143903 (2006)
95. R. Agarwal, C.J. Barrelet, C.M. Lieber, Lasing in single cadmium sulfide nanowire optical cavities. Nano Lett. **5**(5), 917–920 (2005)
96. A.B. Greytak, C.J. Barrelet, Y. Li, C.M. Lieber, Semiconductor nanowire laser and nanowire waveguide electro-optic modulators. Appl. Phys. Lett. **87**(15), 151103 (2005)
97. B. Liu, R. Chen, X. Xu, D. Li, Y. Zhao, Z. Shen, Q. Xiong, H. Sun, Exciton-related photoluminescence and lasing in CdS nanobelts. J. Phys. Chem. C **115**(26), 12826–12830 (2011)
98. S. Geburt, A. Thielmann, R. Röder, C. Borschel, A. McDonnell, M. Kozlik, J. Kühnel, K.A. Sunter, F. Capasso, C. Ronning, Low threshold room-temperature lasing of CdS nanowires. Nanotechnology **23**(36), 365204 (2012)
99. A. Pan, R. Liu, Q. Zhang, Q. Wan, P. He, M. Zacharias, B. Zou, Fabrication and red-color lasing of individual highly uniform single-crystal CdSe nanobelts. J. Phys. Chem. C **111**(38), 14253–14256 (2007)
100. Y. Ye, Y. Ma, S. Yue, L. Dai, H. Meng, Z. Li, L. Tong, G. Qin, Lasing of CdSe/SiO2 nanocables synthesized by the facile chemical vapor deposition method. Nanoscale **3**(8), 3072–3075 (2011)
101. A. Chin, S. Vaddiraju, A. Maslov, C. Ning, M. Sunkara, M. Meyyappan, Near-infrared semiconductor subwavelength-wire lasers. Appl. Phys. Lett. **88**(16), 163115 (2006)
102. B. Hua, J. Motohisa, Y. Ding, S. Hara, T. Fukui, Characterization of Fabry-Perot microcavity modes in GaAs nanowires fabricated by selective-area metal organic vapor phase epitaxy. Appl. Phys. Lett. **91**(13), 131112 (2007)

103. Y. Ding, J. Motohisa, B. Hua, S. Hara, T. Fukui, Observation of microcavity modes and waveguides in InP nanowires fabricated by selective-area metalorganic vapor-phase epitaxy. Nano Lett. **7**(12), 3598–3602 (2007)
104. B. Hua, J. Motohisa, Y. Kobayashi, S. Hara, T. Fukui, Single GaAs/GaAsP coaxial core-shell nanowire lasers. Nano Lett. **9**(1), 112–116 (2009)
105. Y. Liu, J.A. Zapien, Y. Shan, C.Y. Geng, C.S. Lee, S.T. Lee, Wavelength-controlled lasing in $Zn_xCd_{1-x}S$ single-crystal nanoribbons. Adv. Mater. **17**(11), 1372–1377 (2005)
106. A. Pan, H. Yang, R. Liu, R. Yu, B. Zou, Z. Wang, Color-tunable photoluminescence of alloyed CdS_xSe_{1-x} nanobelts. J. Am. Chem. Soc. **127**(45), 15692–15693 (2005)
107. A. Pan, R. Liu, F. Wang, S. Xie, B. Zou, M. Zacharias, Z.L. Wang, High-QUALITY ALLOYED $CdS_xSe_{1\text{-}x}$ whiskers as waveguides with tunable stimulated emission. J. Phys. Chem. B **110**(45), 22313–22317 (2006)
108. Y. Liu, J. Zapien, Y. Shan, H. Tang, C. Lee, S. Lee, Wavelength-tunable lasing in single-crystal $CdS_{1-X}Se_X$ nanoribbons. Nanotechnology **18**(36), 365606 (2007)
109. A. Pan, W. Zhou, E.S. Leong, R. Liu, A.H. Chin, B. Zou, C. Ning, Continuous alloy-composition spatial grading and superbroad wavelength-tunable nanowire lasers on a single chip. Nano Lett. **9**(2), 784–788 (2009)
110. F. Gu, Z. Yang, H. Yu, J. Xu, P. Wang, L. Tong, A. Pan, Spatial bandgap engineering along single alloy nanowires. J. Am. Chem. Soc. **133**(7), 2037–2039 (2011)
111. J. Zapien, Y. Liu, Y. Shan, H. Tang, C. Lee, S. Lee, Continuous near-infrared-to-ultraviolet lasing from II-VI nanoribbons. Appl. Phys. Lett. **90**(21), 213114 (2007)
112. C. Luan, Y. Liu, Y. Jiang, J. Jie, I. Bello, S. Lee, J. Zapien, Composition tuning of room-temperature nanolasers. Vacuum **86**(6), 737–741 (2012)
113. J. Xu, L. Ma, P. Guo, X. Zhuang, X. Zhu, W. Hu, X. Duan, A. Pan, Room-temperature dual-wavelength lasing from single-nanoribbon lateral heterostructures. J. Am. Chem. Soc. **134**(30), 12394–12397 (2012)
114. H. Zhu, Y. Fu, F. Meng, X. Wu, Z. Gong, Q. Ding, M.V. Gustafsson, M.T. Trinh, S. Jin, X. Zhu, Lead halide perovskite nanowire lasers with low lasing thresholds and high quality factors. Nat. Mater. **14**(6), 636–642 (2015)
115. Y. Xiao, C. Meng, P. Wang, Y. Ye, H. Yu, S. Wang, F. Gu, L. Dai, L. Tong, Single-nanowire single-mode laser. Nano Lett. **11**(3), 1122–1126 (2011)
116. Y. Xiao, C. Meng, X. Wu, L. Tong, Single mode lasing in coupled nanowires. Appl. Phys. Lett. **99**(2), 023109 (2011)
117. H. Xu, J.B. Wright, T.-S. Luk, J.J. Figiel, K. Cross, L.F. Lester, G. Balakrishnan, G.T. Wang, I. Brener, Q. Li, Single-mode lasing of GaN nanowire-pairs. Appl. Phys. Lett. **101**(11), 113106 (2012)
118. H. Gao, A. Fu, S.C. Andrews, P. Yang, Cleaved-coupled nanowire lasers. Proc. Natl. Acad. Sci. U.S.A. **110**(3), 865–869 (2013)
119. X. Duan, Y. Huang, R. Agarwal, C.M. Lieber, Single-nanowire electrically driven lasers. Nature **421**(6920), 241–245 (2003)
120. X. Ma, J. Pan, P. Chen, D. Li, H. Zhang, Y. Yang, D. Yang, Room temperature electrically pumped ultraviolet random lasing from ZnO nanorod arrays on Si. Opt. Express **17**(16), 14426–14433 (2009)
121. S. Chu, G. Wang, W. Zhou, Y. Lin, L. Chernyak, J. Zhao, J. Kong, L. Li, J. Ren, J. Liu, Electrically pumped waveguide lasing from ZnO nanowires. Nat. Nanotechnol. **6**(8), 506–510 (2011)
122. C. Liu, H. Xu, J. Ma, X. Li, X. Zhang, Y. Liu, R. Mu, Electrically pumped near-ultraviolet lasing from ZnO/MgO core/shell nanowires. Appl. Phys. Lett. **99**(6), 063115 (2011)
123. X.-Y. Liu, C.-X. Shan, S.-P. Wang, Z.-Z. Zhang, D.-Z. Shen, Electrically pumped random lasers fabricated from ZnO nanowire arrays. Nanoscale **4**(9), 2843–2846 (2012)
124. K. Li, X. Liu, Q. Wang, S. Zhao, Z. Mi, Ultralow-threshold electrically injected AlGaN nanowire ultraviolet lasers on Si operating at low temperature. Nat. Nanotechnol. **10**(2), 140–144 (2015)

125. F. Omnes, Introduction to semiconductor photodetectors. In *Optoelectronic Sensors* (ISTE, Arlington, VA, 2010), pp. 1–14
126. H. Kind, H. Yan, B. Messer, M. Law, P. Yang, Nanowire Ultraviolet Photodetectors and Optical Switches. Adv. Mater. **14**(2), 158–160 (2002)
127. C. Soci, A. Zhang, X.-Y. Bao, H. Kim, Y. Lo, D. Wang, Nanowire photodetectors. J. Nanosci. Nanotechnol. **10**(3), 1430–1449 (2010)
128. M. Son, S. Im, Y. Park, C. Park, T. Kang, K.-H. Yoo, Ultraviolet photodetector based on single GaN nanorod p–n junctions. Mater. Sci. Eng., C **26**(5), 886–888 (2006)
129. H. Pettersson, J. Trägårdh, A.I. Persson, L. Landin, D. Hessman, L. Samuelson, Infrared photodetectors in heterostructure nanowires. Nano Lett. **6**(2), 229–232 (2006)
130. Z. Guo, D. Zhao, Y. Liu, D. Shen, J. Zhang, B. Li, Visible and ultraviolet light alternative photodetector based on ZnO nanowire/n-Si heterojunction. Appl. Phys. Lett. **93**(16), 163501–163501-3 (2008)
131. O. Hayden, R. Agarwal, C.M. Lieber, Nanoscale avalanche photodiodes for highly sensitive and spatially resolved photon detection. Nat. Mater. **5**(5), 352–356 (2006)
132. C. Yang, C.J. Barrelet, F. Capasso, C.M. Lieber, Single p-type/intrinsic/n-type silicon nanowires as nanoscale avalanche photodetectors. Nano Lett. **6**(12), 2929–2934 (2006)
133. Y. Ahn, J. Dunning, J. Park, Scanning photocurrent imaging and electronic band studies in silicon nanowire field effect transistors. Nano Lett. **5**(7), 1367–1370 (2005)
134. Y. Gu, E.-S. Kwak, J. Lensch, J. Allen, T.W. Odom, L.J. Lauhon, Near-field scanning photocurrent microscopy of a nanowire photodetector. Appl. Phys. Lett. **87**(4), 043111 (2005)
135. G. Cheng, X. Wu, B. Liu, B. Li, X. Zhang, Z. Du, ZnO nanowire Schottky barrier ultraviolet photodetector with high sensitivity and fast recovery speed. Appl. Phys. Lett. **99**(20), 203105 (2011)
136. A. Fujiwara, K. Yamazaki, Y. Takahashi, Detection of single charges and their generation-recombination dynamics in Si nanowires at room temperature. Appl. Phys. Lett. **80**(24), 4567–4569 (2002)
137. Y. Ahn, J. Park, Efficient visible light detection using individual germanium nanowire field effect transistors. Appl. Phys. Lett. **91**(16), 162102 (2007)
138. J.K. Yang, E. Dauler, A. Ferri, A. Pearlman, A. Verevkin, G. Gol'tsman, B. Voronov, R. Sobolewski, W.E. Keicher, K.K. Berggren, Fabrication development for nanowire GHz-counting-rate single-photon detectors. IEEE T. Appl. Supercon. **15**(2), 626–630 (2005)
139. K.M. Rosfjord, J.K. Yang, E.A. Dauler, A.J. Kerman, V. Anant, B.M. Voronov, G.N. Gol'Tsman, K.K. Berggren, Nanowire single-photon detector with an integrated optical cavity and anti-reflection coating. Opt. Express **14**(2), 527–534 (2006)
140. F. Marsili, D. Bitauld, A. Fiore, A. Gaggero, F. Mattioli, R. Leoni, M. Benkahoul, F. Lévy, High efficiency NbN nanowire superconducting single photon detectors fabricated on MgO substrates from a low temperature process. Opt. Express **16**(5), 3191–3196 (2008)
141. S. Miki, M. Fujiwara, M. Sasaki, B. Baek, A.J. Miller, R.H. Hadfield, S.W. Nam, Z. Wang, Large sensitive-area NbN nanowire superconducting single-photon detectors fabricated on single-crystal MgO substrates. Appl. Phys. Lett. **92**(6), 061116 (2008)
142. F. Marsili, F. Najafi, E. Dauler, F. Bellei, X. Hu, M. Csete, R.J. Molnar, K.K. Berggren, Single-photon detectors based on ultranarrow superconducting nanowires. Nano Lett. **11**(5), 2048–2053 (2011)
143. S. Ferrari, O. Kahl, V. Kovalyuk, G.N. Goltsman, A. Korneev, W.H. Pernice, Waveguide-integrated single-and multi-photon detection at telecom wavelengths using superconducting nanowires. Appl. Phys. Lett. **106**(15), 151101 (2015)
144. C.M. Natarajan, M.G. Tanner, R.H. Hadfield, Superconducting nanowire single-photon detectors: physics and applications. Supercond. Sci. Technol. **25**(6), 063001 (2012)